

# Pulsed coherent Rydberg excitation in a thermal gas of Rubidium

Diplomarbeit von  
Michael Schlagmüller  
20.08.2011

Hauptberichter: Prof. Dr. Tilman Pfau  
Mitberichter: Prof. Dr. Harald Giessen

**Universität Stuttgart**  
**5. Physikalisches Institut**



## Abstract

In this thesis the observation of gigahertz Rabi oscillations to a Rydberg state in a thermal gas of rubidium is presented. A two photon excitation scheme is used of which the excitation to the Rydberg state is driven by a pulsed laser. During the time of the pulse ( $\sim 4$  ns) six full Rabi cycles were achieved with a peak Rabi frequency of  $\sim 2.3$  GHz. All experimental data presented is in good agreement with a model of non-interacting three-level atoms and will be discussed in detail.

The fully coherent dynamics shown in the experiment paves the way towards the realization of quantum devices at room temperature such as single photon sources or quantum gates.

Parts of the results of this thesis are published in:

Phys. Rev. Lett. 107, 243001 (2011)

B. Huber, T. Baluktsian, M. Schlagmüller, A. Kölle, H. Kübler, R. Löw and T. Pfau  
GHz Rabi flopping to Rydberg states in hot atomic vapor cells

## Declaration

I hereby declare that this submission is my own work and that, to the best of my knowledge and belief, it contains no material previously published or written by another person, except where due acknowledgment has been made in the text.

Michael Schlagmüller

Stuttgart, August 20, 2011

# Contents

<b>1. Introduction</b>	<b>5</b>
<b>2. Theoretical foundations</b>	<b>6</b>
2.1. Rydberg atoms . . . . .	6
2.2. Atom light interaction . . . . .	7
2.2.1. Two-level atoms . . . . .	7
2.2.2. Rotating wave approximation . . . . .	9
2.2.3. Three-level atoms . . . . .	10
2.2.4. Autler-Townes splitting . . . . .	12
2.3. Optical properties . . . . .	17
<b>3. Experimental setup</b>	<b>20</b>
3.1. DAVLL spectroscopy . . . . .	21
3.2. EIT spectroscopy . . . . .	23
3.3. Pulsed laser setup . . . . .	25
3.4. Setup for Rydberg excitation . . . . .	27
<b>4. Experimental results</b>	<b>30</b>
4.1. Experimental parameters . . . . .	30
4.2. Rabi oscillations . . . . .	32
4.2.1. Rabi oscillations for different pulse intensities . . . . .	33
4.2.2. Rabi oscillations for different pulse detunings . . . . .	33
<b>5. Simulation and discussion</b>	<b>36</b>
5.1. Rabi oscillations for different pulse intensities . . . . .	39
5.2. Rabi oscillations for different pulse detunings . . . . .	39
5.2.1. Autler-Townes splitting . . . . .	42
5.2.2. Pulse shape dependence . . . . .	46
5.2.3. Angular dependence . . . . .	49
5.2.4. Temperature dependence . . . . .	50
5.3. Further development . . . . .	51
<b>6. Summary and Outlook</b>	<b>53</b>
<b>A. Level scheme and <math>D_1/D_2</math> absorption spectrum of Rubidium</b>	<b>56</b>
<b>B. Simulation details</b>	<b>59</b>

# 1. Introduction

About 100 years ago, a new field of research arose: quantum mechanics. This field of study founded a new age to come in physics. At first quantum mechanics was invented and developed to explain observations like black body radiation, which could not be explained with the existing classical theories. Soon after, famous people like Planck, Born, Bohr, Schrödinger and Heisenberg were giving a shape to the theory. With this development a fundamental understanding for the basic components of physics like atoms, electrons and photons and their interactions with one another was established. Quantum mechanics shows the beauty of physics: with only a few basic postulates a vast range of phenomena can be explained.

On the foundation of quantum mechanics the still upcoming field of quantum information processing was developed. In 1982 Richard Feynman was one of the first to suggest using quantum systems for quantum simulations [1] and in 1985 David Deutsch described the concept of a universal quantum computer [2]. It was shown that some time-consuming issues like simulating quantum systems or factoring numbers would speed up significantly using quantum information processing (e.g. Shor's algorithm [3]). Up to now only proof-of-concept experiments with a few qubits, the quantum analogon of classical bits, could be realized implementing quantum algorithms. Although various quantum systems like ion traps [4], nuclear spins [5], electron spins [6], quantum dots [7] and others were proposed and realized, all of them lack of scalability.

A new way of realizing a quantum system with a fair chance towards scalability [8] makes use of Rydberg states in a thermal rubidium vapor. The focus of this thesis is first to show the experimental results of coherent Rydberg excitations in a thermal gas of rubidium and second to present a detailed study of the physics involved. Even though the coherence time of this system is in the range of a couple of nanoseconds the coherent dynamics could be observed by driving the Rydberg transition on the low gigahertz scale. This is a promising first step towards a realization of scalable quantum devices. Various applications in quantum information processing have been proposed for Rydberg atoms [9, 10, 11].

## 2. Theoretical foundations

This chapter gives an introduction into the theoretical foundations required to explain and discuss the observed phenomena of the experiment. As these topics have been addressed in books, articles and theses, the explanations presented in this chapter are based on this literature, taken, modified and extended for the purpose of this thesis. The sources for the different sections are the following: 2.1 Rydberg atoms: J. Pritchard [12], 2.2.4 Autler-Townes splitting: C. Cohen-Tannoudji [13], 3 Experimental setup: E. Bäder [14] and S. Müller [15].

### 2.1. Rydberg atoms

The main property which defines a Rydberg atom is a highly excited electron with a large principal quantum number  $n$ . The Rydberg series was originally identified in the spectral lines of atomic hydrogen where the binding energy  $W$  was found empirically to be related to the formula

$$W = -\frac{\text{Ry}}{n^2}, \quad (2.1)$$

where Ry was a constant and  $n$  an integer. The theoretical underpinning for this scaling arrived with the Bohr model of the atom in 1913 [16], from which the Rydberg constant Ry could be derived in terms of fundamental constants

$$\text{Ry} = \frac{e^4 m_e}{8\epsilon_0^2 h^2} \quad (2.2)$$

and  $n$  understood as the principal quantum number. From the Bohr model it was also possible to derive scaling laws for the atomic properties in terms of  $n$ , which were later verified and extended by the full quantum mechanical treatment of Schrödinger in 1926 [17]. Table 2.1 summarizes the scaling laws of the atomic properties for the low- $\ell$  Rydberg states. One property is the large orbital radius, another one the scaling law of the polarizability with  $n^7$ . The consequence of the large polarizability is an enormous response to external

fields and the ability to observe dipole-dipole interactions between atoms on the  $\mu\text{m}$  scale for  $n \approx 50$ . Combining this with the relatively long lifetimes compared to ground state transitions, Rydberg atoms are well suited for applications in coherent quantum gates [11].

property	$n$ -scaling
energy difference of adjacent $n$ states	$n^{-3}$
binding energy $W$	$n^{-2}$
orbital radius $\langle r \rangle$	$n^2$
radiative lifetime $\tau$	$n^3$
polarizability	$n^7$

Table 2.1.: Scaling laws for properties of the Rydberg states [18].

## 2.2. Atom light interaction

The simplest case to consider the interaction between atoms and light is that of a two-level atom driven by a coherent optical field. This system has been exhaustively studied (e.g. [19, 20]), revealing a range of coherent effects such as Rabi oscillations [21]. However, the addition of a third level and a second light field gives rise to a range of coherent phenomena.

### 2.2.1. Two-level atoms

In order to handle the interaction between two electronic states of an atom and a light field, the level structure of an atom can be reduced to a simple two-level system (see figure 2.1). The two different states are described by

$$|g\rangle := \begin{pmatrix} 1 \\ 0 \end{pmatrix} \quad \text{and} \quad |e\rangle := \begin{pmatrix} 0 \\ 1 \end{pmatrix}. \quad (2.3)$$

The corresponding Hamiltonian without light and an energy difference of  $\hbar\Delta_{ge}$  between the ground and the excited state can be written as

$$H_0 = \hbar \begin{pmatrix} 0 & 0 \\ 0 & \Delta_{ge} \end{pmatrix}. \quad (2.4)$$

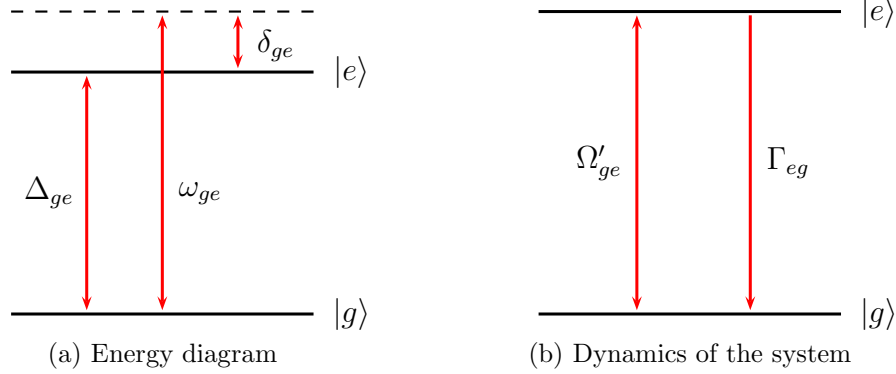


Figure 2.1.: Overview of the two-level scheme: a) Energy levels with resonance frequency  $\Delta_{ge}$  of the ground to the excited state, light frequency  $\omega_{ge}$  and detuning  $\delta_{ge}$ . b) Dynamic between the states involved is described by the effective Rabi frequency  $\Omega'_{ge}$  and the decay rate  $\Gamma_{eg}$ .

With a classical light field interaction turned on, the corresponding Hamiltonian has to be modified to

$$H = H_0 + V_{\text{al}} = \hbar \begin{pmatrix} 0 & 0 \\ 0 & \Delta_{ge} \end{pmatrix} + \begin{pmatrix} 0 & -d_{ge}E(t) \\ -d_{ge}E(t) & 0 \end{pmatrix} \quad (2.5)$$

whereas  $V_{\text{al}}$  describes the atom light interaction and  $d_{ge}$  the dipole matrix element. The light field is expressed by a plane wave  $E(t) = E_0(e^{i\omega_{ge}t} + e^{-i\omega_{ge}t})/2$ .

The Rabi frequency

$$\Omega_{ge} := -\frac{d_{ge}E_0}{\hbar}. \quad (2.6)$$

is introduced to simplify the Hamiltonian to

$$H = \hbar \begin{pmatrix} 0 & (e^{i\omega_{ge}t} + e^{-i\omega_{ge}t}) \Omega_{ge}/2 \\ (e^{i\omega_{ge}t} + e^{-i\omega_{ge}t}) \Omega_{ge}/2 & \Delta_{ge} \end{pmatrix}. \quad (2.7)$$

The time evolution of the density matrix is described by the von Neumann equation

$$\frac{\partial \rho}{\partial t} = -\frac{i}{\hbar}[H, \rho], \quad (2.8)$$

which is an equivalent to the Schrödinger equation.

The corresponding density matrix is defined as

$$\rho := \begin{pmatrix} \rho_{gg} & \rho_{ge} \\ \rho_{eg} & \rho_{ee} \end{pmatrix}. \quad (2.9)$$



The diagonal entries represent the population of the states. The off-diagonal entries are called the coherences.

Up to now we have neglected dissipative effects. For this we have to add the Lindblad operator  $\mathcal{L}_D$ . The full dynamics is described by the Liouville-von Neumann equation

$$\frac{\partial \rho}{\partial t} = -\frac{i}{\hbar}[H, \rho] + \mathcal{L}_D(\rho), \quad (2.10)$$

whereas the Lindblad operator is defined by [22]

$$\mathcal{L}_D := \frac{1}{2} \sum_j \left( [C_j \rho, C_j^\dagger] + [C_j, \rho C_j^\dagger] \right). \quad (2.11)$$

The index  $j$  denotes the different possible decay channels. The Lindblad operator describes the coupling to the vacuum modes. Performing the calculation preceding for a two-level system, where only one decay channel  $C_1 = \sqrt{\Gamma_{eg}} |g\rangle \langle e|$  is available, we see that the excited state decays with the corresponding decay rate  $\Gamma_{eg}$  and the coherences decay with  $\Gamma_{eg}/2$ . So we finally obtain

$$\mathcal{L}_D = \Gamma_{eg} \begin{pmatrix} \rho_{ee} & -\frac{1}{2}\rho_{ge} \\ -\frac{1}{2}\rho_{eg} & -\rho_{ee} \end{pmatrix}. \quad (2.12)$$

### 2.2.2. Rotating wave approximation

In order to simplify the equations, the system is transformed in a frame that is rotating with the frequency of the light  $\omega_{ge}$ .

We start from the Hamiltonian of equation (2.7):

$$H = \hbar \begin{pmatrix} 0 & (e^{i\omega_{ge}t} + e^{-i\omega_{ge}t}) \Omega_{ge}/2 \\ (e^{i\omega_{ge}t} + e^{-i\omega_{ge}t}) \Omega_{ge}/2 & \Delta_{ge} \end{pmatrix}$$

The transformation into a rotated frame is given by the unitary matrix

$$U := \begin{pmatrix} 1 & 0 \\ 0 & e^{-i\omega_{ge}t} \end{pmatrix}. \quad (2.13)$$

Hence the density matrix is transformed by

$$\rho_R = U^\dagger \rho U = \begin{pmatrix} \rho_{gg} & \rho_{ge} e^{-i\omega_{ge}t} \\ \rho_{eg} e^{i\omega_{ge}t} & \rho_{ee} \end{pmatrix} \quad (2.14)$$

and leads to the transformed Hamilton operator in the rotating frame

$$H_R = U^\dagger H U - i\hbar U^\dagger \frac{\partial U}{\partial t} = \hbar \begin{pmatrix} 0 & (1 + e^{-2i\omega_{ge}t}) \Omega_{ge}/2 \\ (1 + e^{2i\omega_{ge}t}) \Omega_{ge}/2 & -(\omega_{ge} - \Delta_{ge}) \end{pmatrix}. \quad (2.15)$$

The rotating wave approximation implies that the fast light frequency  $\omega_{ge}$  averages to zero over the interaction time and can thus be neglected. Together with the detuning  $\delta_{ge} := \omega_{ge} - \Delta_{ge}$  the equation can be simplified to

$$H_{\text{RWA}} = \hbar \begin{pmatrix} 0 & \Omega_{ge}/2 \\ \Omega_{ge}/2 & -\delta_{ge} \end{pmatrix}. \quad (2.16)$$

By calculating the eigenvalues of the Hamiltonian, which include the atom and the light field, the energies of the so-called dressed states yield

$$E_{1/2} = \frac{\hbar}{2} \left( \delta_{ge} \pm \sqrt{\Omega_{ge}^2 + \delta_{ge}^2} \right). \quad (2.17)$$

This results in the oscillation frequency of the population (generalized Rabi frequency) of the two involved states:

$$\Omega'_{ge} = \frac{E_1 - E_2}{\hbar} = \sqrt{\Omega_{ge}^2 + \delta_{ge}^2}. \quad (2.18)$$

### 2.2.3. Three-level atoms

The addition of a third level  $|r\rangle$  and a second light field  $\omega_{er}$  is a simple extension to the two-level system but gives rise to a lot of new phenomena.

We are considering a three-level system now consisting of a ground state  $|g\rangle$ , an excited state  $|e\rangle$  and a Rydberg state  $|r\rangle$  as shown in figure 2.2

$$|g\rangle := \begin{pmatrix} 1 \\ 0 \\ 0 \end{pmatrix}, |e\rangle := \begin{pmatrix} 0 \\ 1 \\ 0 \end{pmatrix}, |r\rangle := \begin{pmatrix} 0 \\ 0 \\ 1 \end{pmatrix}, \quad (2.19)$$

which is interacting with a light field  $E_{ge}(t) := E_{0,ge}(e^{i\omega_{ge}t} + e^{-i\omega_{ge}t})/2$  coupling the ground state to the excited state, and a second light field  $E_{er}(t) := E_{0,er}(e^{i\omega_{er}t} + e^{-i\omega_{er}t})/2$  coupling the excited state to the Rydberg state. In analogy to equation (2.5) the Hamiltonian  $H$

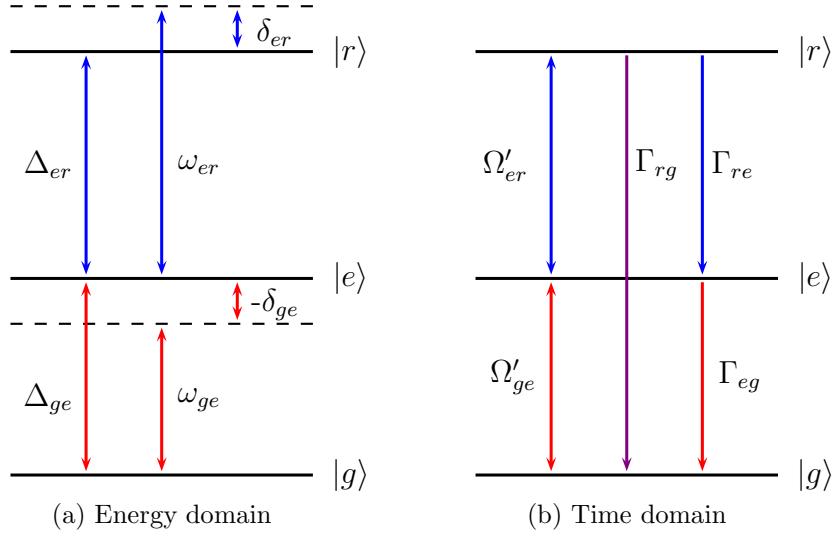


Figure 2.2.: Overview over the three-level scheme: a) Energy levels and resonance frequencies  $\Delta_{ge}$  and  $\Delta_{er}$ , light frequencies  $\omega_{ge}$  and  $\omega_{er}$  and detunings  $\delta_{ge}$  and  $\delta_{er}$ . b) Dynamic between the involved states is described by the effective Rabi frequencies  $\Omega'_{ge}$  and  $\Omega'_{er}$  and the decay rates  $\Gamma_{eg}, \Gamma_{re}$  and  $\Gamma_{rg}$ .

has the form

$$H = \begin{pmatrix} 0 & -d_{ge}E_{ge}(t) & 0 \\ -d_{ge}E_{ge}(t) & \hbar\Delta_{ge} & -d_{er}E_{er}(t) \\ 0 & -d_{er}E_{er}(t) & \hbar(\Delta_{ge} + \Delta_{er}) \end{pmatrix}. \quad (2.20)$$

The corresponding unitary matrix for the rotating frame transformation is

$$U = \begin{pmatrix} 1 & 0 & 0 \\ 0 & e^{-i\omega_{ge}t} & 0 \\ 0 & 0 & e^{-i(\omega_{ge}+\omega_{er})t} \end{pmatrix}. \quad (2.21)$$

Applying the rotating wave approximation, we find

$$H_{\text{RWA}} = \hbar \begin{pmatrix} 0 & \Omega_{ge}/2 & 0 \\ \Omega_{ge}/2 & -\delta_{ge} & \Omega_{er}/2 \\ 0 & \Omega_{er}/2 & -\delta_{ge} - \delta_{er} \end{pmatrix}, \quad (2.22)$$

where we used the definitions  $\delta_{ge} := \omega_{ge} - \Delta_{ge}$  and  $\delta_{er} := \omega_{er} - \Delta_{er}$ . The transformed

density matrix for a three-level system is given by

$$\rho_R = \begin{pmatrix} \rho_{gg} & \rho_{ge}e^{i\omega_{ge}t} & \rho_{gr}e^{i(\omega_{ge}+\omega_{er})t} \\ \rho_{eg}e^{-i\omega_{ge}t} & \rho_{ee} & \rho_{er}e^{i\omega_{er}t} \\ \rho_{rg}e^{-i(\omega_{ge}+\omega_{er})t} & \rho_{re}e^{-i\omega_{er}t} & \rho_{rr} \end{pmatrix}. \quad (2.23)$$

If all decay channels are allowed the Lindblad operator follows as

$$\begin{aligned} \mathcal{L}_D = & \Gamma_{re} \begin{pmatrix} 0 & 0 & -\frac{1}{2}\tilde{\rho}_{gr} \\ 0 & \tilde{\rho}_{rr} & -\frac{1}{2}\tilde{\rho}_{er} \\ -\frac{1}{2}\tilde{\rho}_{gr} & -\frac{1}{2}\tilde{\rho}_{re} & -\tilde{\rho}_{rr} \end{pmatrix} \\ & + \Gamma_{rg} \begin{pmatrix} \tilde{\rho}_{rr} & 0 & -\frac{1}{2}\tilde{\rho}_{gr} \\ 0 & 0 & -\frac{1}{2}\tilde{\rho}_{er} \\ -\frac{1}{2}\tilde{\rho}_{gr} & -\frac{1}{2}\tilde{\rho}_{re} & -\tilde{\rho}_{rr} \end{pmatrix} \\ & + \Gamma_{eg} \begin{pmatrix} \tilde{\rho}_{ee} & -\frac{1}{2}\tilde{\rho}_{ge} & 0 \\ -\frac{1}{2}\tilde{\rho}_{eg} & -\tilde{\rho}_{ee} & -\frac{1}{2}\tilde{\rho}_{er} \\ 0 & -\frac{1}{2}\tilde{\rho}_{re} & 0 \end{pmatrix}. \end{aligned} \quad (2.24)$$

#### 2.2.4. Autler-Townes splitting

In a three-level system (figure 2.3), where two levels are strongly coupled due to a light field, the dressed state picture can be used to explain the observable phenomena. The coupled system 'atom + driving photons' is called 'dressed atom'. In particular as it will be shown in the following, the Autler-Townes effect is associated with a level anticrossing in the corresponding energy diagram.

Let us assume that the upper excitation from  $|e\rangle$  to  $|r\rangle$  is strongly coupled by a light field  $\omega_{er}$  and the lower excitation light  $\omega_{ge}$  is weak and out of resonance for the upper transition and hence can be neglected for the calculation of the dressed state. The uncoupled states which interact are described by

$$\begin{aligned} |e, N+1\rangle & \text{ atom in the excited state } e \text{ in the presence of } N+1 \text{ photons } \omega_{er}, \\ |r, N\rangle & \text{ atom in the Rydberg state } r \text{ with } N \text{ photons } \omega_{er}. \end{aligned}$$

The energy difference between the two states follows as

$$\Delta E = \left( E_e + (N+1)\hbar\omega_{er} \right) - \left( E_r + N\hbar\omega_{er} \right) = \hbar(\omega_{er} - \Delta_{er}) = \hbar\delta_{er}. \quad (2.25)$$

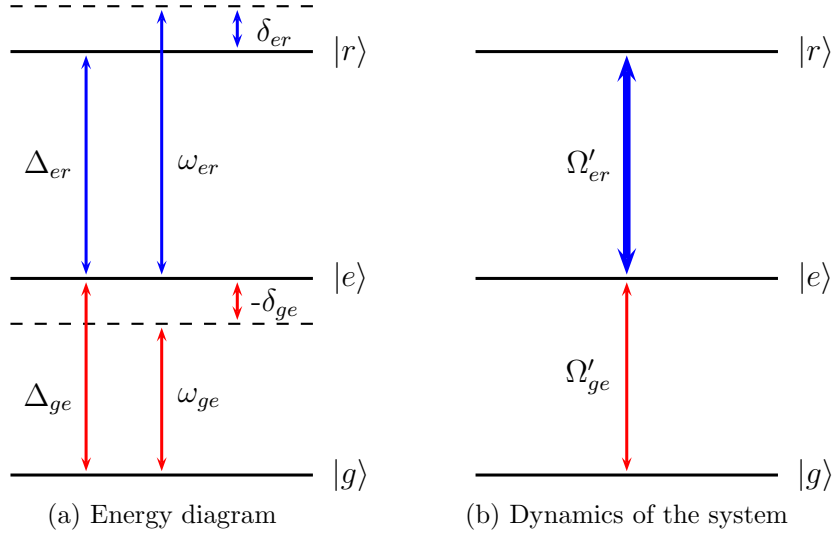


Figure 2.3.: Overview over the considered three-level scheme: a) Energy levels and resonance frequencies  $\Delta_{ge}$  and  $\Delta_{er}$ , light frequencies  $\omega_{ge}$  and  $\omega_{er}$  and detunings  $\delta_{ge}$  and  $\delta_{er}$ . b) Dynamic between the involved states is described by the effective Rabi frequencies  $\Omega'_{ge}$  and  $\Omega'_{er}$ .

At resonance ( $\delta_{er} = 0$ ) the levels  $|e, N + 1\rangle$  and  $|r, N\rangle$  are degenerate. As a result of the coupling, the two states  $|e, N + 1\rangle$  and  $|r, N\rangle$  repel each other and form a lower and upper perturbed or dressed state  $|L\rangle$  and  $|U\rangle$ , whose energies are separated by a distance  $\hbar\Omega'_{er}$  with

$$\Omega'_{er} = \sqrt{\Omega_{er}^2 + \delta_{er}^2}, \quad (2.26)$$

where  $\Omega'_{er}$  is the effective Rabi frequency (see figure 2.4).

The third state  $|g, N + 1\rangle$  (atom in the ground state  $g$  with  $N + 1$  photons  $\omega_{er}$ ) is not affected by the light coupling  $\omega_{er}$ . The absorption spectrum of a probe field  $\omega_{ge}$ , which would show a single transition at the frequency  $\Delta_{ge}$  in the absence of the coupling light  $\omega_{er}$ , becomes a doublet as soon as the  $e \leftrightarrow r$  transition is driven by the field  $\omega_{er}$ , since both dressed states contain an admixture of  $|e, N + 1\rangle$ . This doublet is called the Autler-Townes doublet. Only at resonance  $\delta_{er} = 0$  the Autler-Townes effect shows a symmetric splitting. With a detuning the frequency shift and the absorption strength changes. The energy

eigenvalues of the dressed states result in

$$E_U = \frac{\hbar}{2}(-\delta_{er} + \sqrt{\delta_{er}^2 + \Omega_{er}^2}) + \Delta_{ge} \quad (2.27)$$

$$E_L = \frac{\hbar}{2}(-\delta_{er} - \sqrt{\delta_{er}^2 + \Omega_{er}^2}) + \Delta_{ge}. \quad (2.28)$$

The absorption strength for the probe transition depends on the projection of the excited state on the dressed state

$$|\langle e | U \rangle|^2 = \frac{1}{2} \left( 1 - \frac{\delta_{er}}{\sqrt{\delta_{er}^2 + \Omega_{er}^2}} \right) \quad (2.29)$$

$$|\langle e | L \rangle|^2 = \frac{1}{2} \left( 1 + \frac{\delta_{er}}{\sqrt{\delta_{er}^2 + \Omega_{er}^2}} \right), \quad (2.30)$$

which is plotted in figure 2.5. An energy diagram of the Autler-Townes splitting, where the anticrossing of the eigenstates is visible, can be seen in figure 2.6. The energy diagram shows how the two components of the Autler-Townes doublet vary with the detuning. On resonance ( $\omega_{er} = \Delta_{er} \rightarrow \delta_{er} = 0$ ), one gets two lines illustrated as red arrows with frequencies

$$\omega_{L,U} = \Delta_{ge} \pm (\Omega_{er}/2). \quad (2.31)$$

The splitting is therefore

$$\Delta E = \hbar \Omega_{er}. \quad (2.32)$$

Far off resonance ( $|\delta_{er}| \gg \Omega_{er}$ ), one of the two lines has an energy close to  $\hbar \Delta_{ge}$ , the other one is close to  $\hbar(\Delta_{ge} + \delta_{er})$ . By evaluating the admixture of  $|e\rangle$  in each dressed state as calculated in equation (2.29) and (2.30), one can determine the absorption strength of both components of the doublet. One finds that they are equal at resonance, whereas the line with an angular frequency close to  $\Delta_{ge}$  becomes the more intense one out of resonance. Note that for large detuning  $|\delta_{er}| \gg \Omega_{er}$ , the distance between each dressed state and its corresponding asymptote is nothing but the ac Stark shift of level  $|e\rangle$  or  $|r\rangle$  due to its coupling with the field  $\omega_{er}$  which is non-resonant.

To clearly see the Autler-Townes effect, it is necessary to work in the strong coupling regime, which means that the Rabi frequency  $\Omega_{er}$  has to be significantly larger than any decay rate of the system. In that case the two lines of the doublet can be resolved, even on resonance.

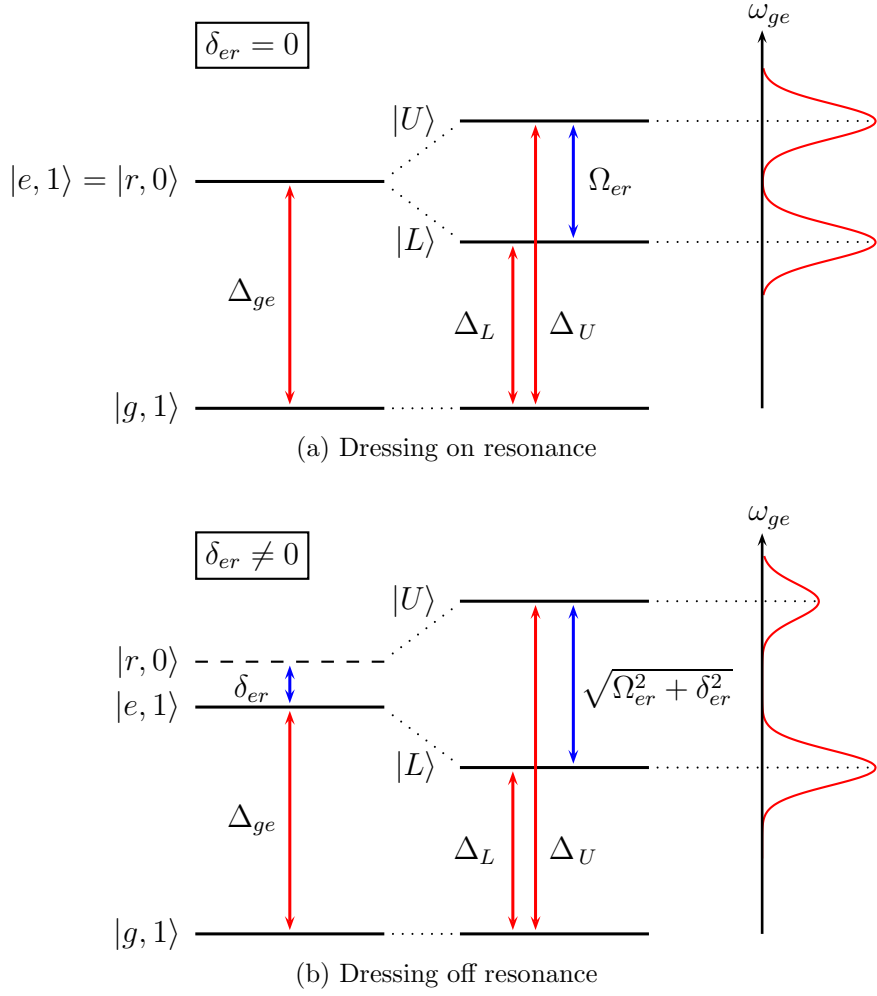


Figure 2.4.: Autler-Townes splitting (a) on resonance and (b) off resonance. On the left hand side the figure shows the uncoupled energies. The center illustrates the dressed eigenstates corresponding to the absorption signal on the right, which shows the Autler-Townes doublet.

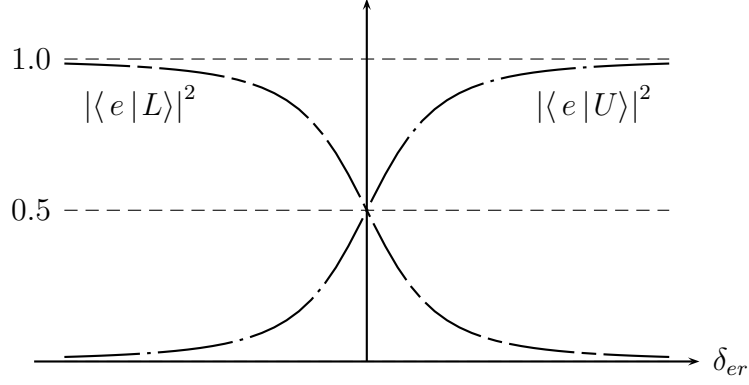


Figure 2.5.: Projection of the excited state to the dressed states which determines the absorptions strength on the lower transition  $g \leftrightarrow e$ .

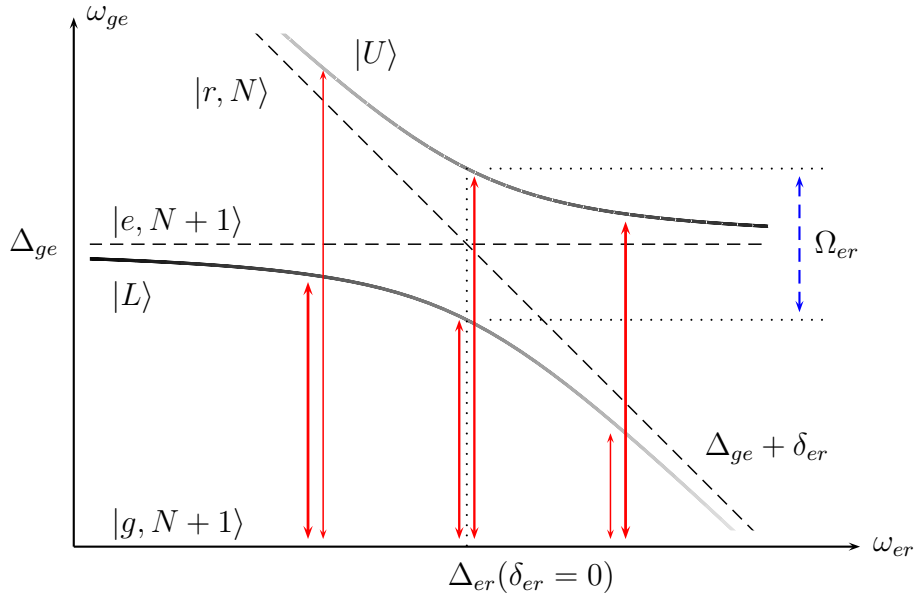


Figure 2.6.: Energy diagram (all frequencies have to be multiplied by  $\hbar$ ) of the dressed states showing the Autler-Townes doublet for variable detuning (x-axis) which is probed by the lower transition (red arrows, y-direction). The projection of the excited state on the dressed states determines the absorptions strength and is indicated by the gray scale value. The dashed lines show the uncoupled states.



### 2.3. Optical properties

For the comparison between the simulations and the experimental data, the imaginary part of the density matrix entry  $\rho_{ge}$  can be connected to the absorption signal in the medium, which will be shown in this section.

The electric field  $E$  and the polarization  $P$  can be expressed as real numbers by satisfying the wave equation for a plane wave as

$$E = \frac{1}{2}(E_{ge} \cdot e^{-i\omega_{ge}t} + E_{ge}^* \cdot e^{i\omega_{ge}t}) \quad (2.33)$$

$$P = \frac{1}{2}(P_0 \cdot e^{-i\omega_{ge}t} + P_0^* \cdot e^{i\omega_{ge}t}). \quad (2.34)$$

The polarization can also be expressed by the atomic density  $n$ , the dipole operator  $d$ , the density matrix  $\rho_{\text{lab}}$  in the laboratory system and the density matrix  $\rho$  in the rotated frame as

$$P = n \text{tr}(d\rho_{\text{lab}}) \quad (2.35)$$

$$= n (\rho_{eg,\text{lab}}d_{ge} + \rho_{ge,\text{lab}}d_{eg}) \quad (2.36)$$

$$= n (\rho_{eg}e^{-i\omega_{ge}t}d_{ge} + \rho_{ge}e^{i\omega_{ge}t}d_{eg}) \quad (2.37)$$

$$= n (\rho_{eg}d_{ge} \cdot e^{-i\omega_{ge}t} + (\rho_{eg}d_{ge})^* \cdot e^{i\omega_{ge}t}). \quad (2.38)$$

By equating coefficients of equation (2.34) and (2.38) the amplitude of the polarization results in

$$P_0 = 2n\rho_{eg}d_{ge}. \quad (2.39)$$

In the slowly varying amplitude approximation [23] the amplitude of the electric field  $E_{ge}(z)$  and the amplitude of the polarization density  $P_0$  are connected by

$$\frac{\partial E_{ge}(z)}{\partial z} = i \frac{\omega_{ge}}{2\epsilon_0 c} P_0. \quad (2.40)$$

Combining the polarization amplitude (2.39) with the partial differential equation leads to

$$\frac{\partial E_{ge}(z)}{\partial z} = i \frac{\omega_{ge}d_{eg}n}{\epsilon_0 c} \rho_{eg}. \quad (2.41)$$

Unfortunately the density matrix  $\rho_{eg}$  depends on the electric field  $E_{ge}$  and hence on the position  $z$ . From simulations it is known that the oscillation frequency of  $\rho_{eg}$  primarily depends on the strongly driven second transition, which is not mentioned yet, and the

influence of the lower transition  $E_{ge}$  can be neglected. Only the amplitude of  $\rho_{eg}$  decreases monotonically over the integration distance by a factor less than two. By neglecting this, the density matrix  $\rho_{eg}$  can be regarded as independent of  $z$ . This approximation allows integrating the partial differential equation over a distance  $\Delta z = z_{\text{out}} - z_{\text{in}}$

$$E_{ge,\text{out}} - E_{ge,\text{in}} = i \frac{\omega_{ge} d_{eg} n \Delta z}{\epsilon_0 C} \rho_{eg} \quad (2.42)$$

$$= i C \rho_{eg} \quad (2.43)$$

with a constant

$$C = \frac{\omega_{ge} d_{eg} n \Delta z}{\epsilon_0 C}. \quad (2.44)$$

Equation (2.43) can be rearranged to

$$E_{ge,\text{out}} = i C \rho_{eg} + E_{ge,\text{in}} \quad (2.45)$$

$$= C(i \text{Re} \rho_{eg} - \text{Im} \rho_{eg}) + E_{ge,\text{in}} \quad (2.46)$$

$$= (E_{ge,\text{in}} - C \text{Im} \rho_{eg}) + i(C \text{Re} \rho_{eg}). \quad (2.47)$$

The outgoing and measured intensity  $I_{ge}$  is proportional to  $|E_{ge}|^2$  and yields

$$|E_{ge,\text{out}}|^2 = E_{ge,\text{in}}^2 - (2 E_{ge,\text{in}} C \text{Im} \rho_{eg}) + (C \text{Im} \rho_{eg})^2 + (C \text{Re} \rho_{eg})^2. \quad (2.48)$$

In order to find which of the terms contribute significantly, each term is evaluated with the parameters used in the experiment:

$$d_{eg} = 1.09 \cdot 10^{-29} \text{ Cm} \quad (\text{see section 3.3})$$

$$\Delta z \simeq 2.5 \text{ mm} \quad (\text{see section 3.4})$$

$$n \simeq 1.3 \cdot 10^{12} \text{ cm}^{-3} \quad (\text{see section 4.1})$$

$$E_{ge,\text{in}} \simeq 1.2 \cdot 10^4 \text{ V/m} \quad (\text{see section 4.2})$$

$$\lambda_{ge} = 780 \text{ nm}$$

$$\omega_{ge} = \frac{2\pi C}{\lambda_{ge}} = 2.4 \cdot 10^{15} \text{ s}^{-1}$$

$$\text{Re} \rho_{eg} \simeq 0.1$$

$$\text{Im} \rho_{eg} \simeq 0.1$$

Hence the terms result in

$$E_{ge,\text{in}}^2 \simeq 14.4 \cdot 10^7 \text{ (V/m)}^2. \quad (2.49)$$

$$2 E_{ge,\text{in}} C \text{Im}\rho_{eg} \simeq 7.7 \cdot 10^7 \text{ (V/m)}^2 \quad (2.50)$$

$$(C \text{Im}\rho_{eg})^2 \simeq 1.0 \cdot 10^7 \text{ (V/m)}^2 \quad (2.51)$$

$$(C \text{Re}\rho_{eg})^2 \simeq 1.0 \cdot 10^7 \text{ (V/m)}^2 \quad (2.52)$$

Since the photodiode is ac coupled, the first term does not contribute to the observed signal. Thus, the leading term by a factor of  $\sim 8$  is the second one which is proportional to  $\text{Im}\rho_{eg}$ . This relation is used to compare the measurements with the simulations. In order to facilitate readability, the simulation of  $\text{Im}\rho_{eg}$  will be called 'simulated absorption signal' in the following.

### 3. Experimental setup

The experiment presented in this thesis realizes coherent Rydberg excitations in a thermal gas of rubidium. The excitation of the Rydberg state is achieved in an effective three-level system coupled with two lasers as shown in figure 3.1. The energy levels involved are the  $5S_{1/2}$ ,  $5P_{3/2}$  and the  $30S_{1/2}$  state, in the following called ground state  $|g\rangle$ , excited state  $|e\rangle$  and Rydberg state  $|r\rangle$  of the isotope  $^{85}\text{Rb}$ . The ground state is coupled to the excited state via a 780 nm cw laser and the upper transition to the Rydberg state is driven by a 480 nm pulsed laser.

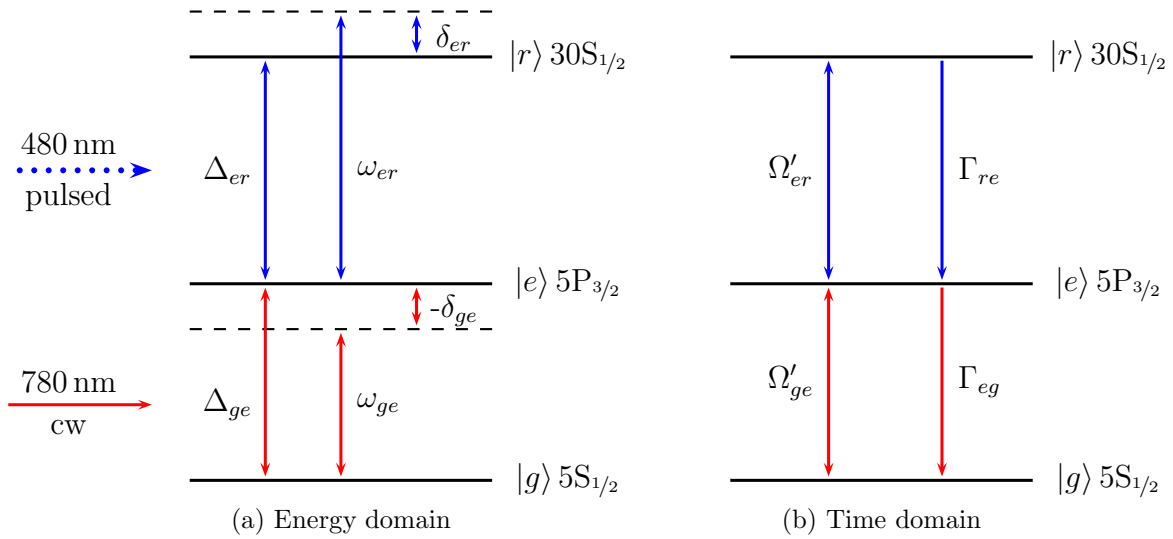


Figure 3.1.: Overview over the three-level scheme: a) Energy levels and resonance frequencies  $\Delta_{ge}$  and  $\Delta_{er}$ , light frequencies  $\omega_{ge}$  and  $\omega_{er}$  and detunings  $\delta_{ge}$  and  $\delta_{er}$ . b) Dynamic between the involved states is described by the effective Rabi frequencies  $\Omega'_{ge}$  and  $\Omega'_{er}$  and the decay rates  $\Gamma_{eg}$  and  $\Gamma_{re}$ .

As the coherence time for the excited state is on the order of 100 nanoseconds [24], Rabi frequencies of at least 100 MHz are required in order to observe coherent excitations in a thermal gas of rubidium. Due to the weak matrix element of the upper transition to the

Rydberg state a high laser intensity is required to drive this transition. Hence, a pulsed laser setup for this excitation is used in the experiment.

To describe the dynamic, at first the cw 780 nm laser drives the lower transition. After the steady state is reached, the blue 480 nm pulse is applied and the population of the three-level system starts to oscillate. To observe the oscillations, the transmission of the 780 nm light is measured.

### 3.1. DAVLL spectroscopy

The 780 nm laser light has to be stabilized to a transition of the ground to the excited state. Thus, the laser is locked by a Doppler-free Dichroic Atomic Vapor Laser Lock (DAVLL) signal via saturation absorption spectroscopy of rubidium atoms in a magnetic field.

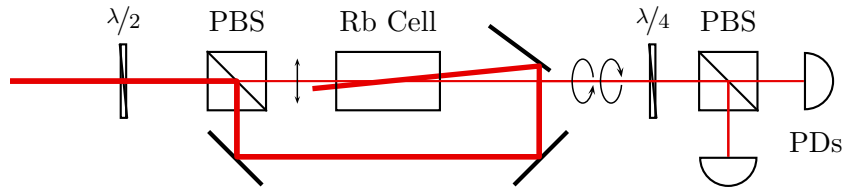


Figure 3.2.: Optical setup for DAVLL spectroscopy for the 780 nm laser lock

The setup is shown in figure 3.2. The beam, which is stabilized, is split into two parts and guided through the rubidium cell in almost counter-propagating direction. When the atoms interact with both beams, the probe and the pump laser, saturation effects are observable in the absorption of the probe laser. So-called Lamb dips occur in the Doppler broadened absorption spectrum exactly at the resonances. Furthermore cross-over resonance dips arise (for details see [25]).

In order to lock the laser, a zero crossing slope is required. Hence a differential signal is used: a magnetic field applied parallel to the propagation direction of the laser splits the atomic state due to the Zeeman shift as demonstrated in figure 3.3. The resonances for the  $\sigma^+$  and  $\sigma^-$  components of the linearly polarized light are detuned by  $\pm\delta(B)$  due to the Zeeman shift. The absorption of a single  $\sigma$  component is plotted over the frequency of the laser in figure 3.4a. The difference of the two shifted amplitudes provides a signal with a steep slope, which is not sensitive to intensity fluctuations of the laser. This is the DAVLL signal shown in figure 3.4b that is used to lock the laser. More details on the DAVLL can be found for example in [26].

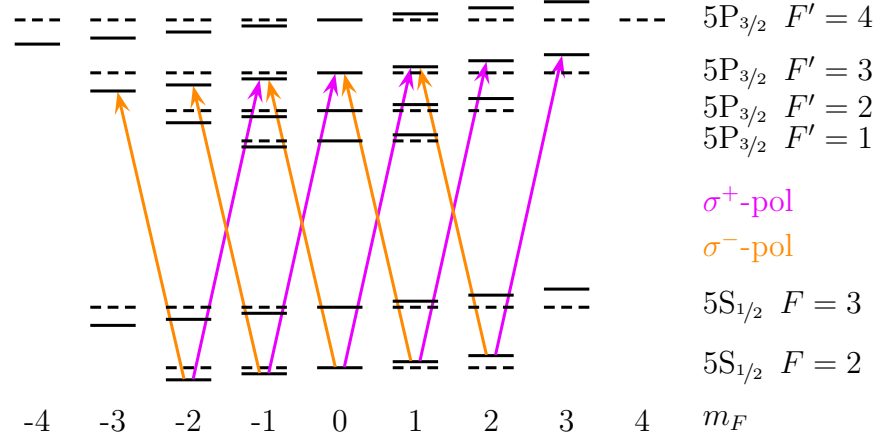
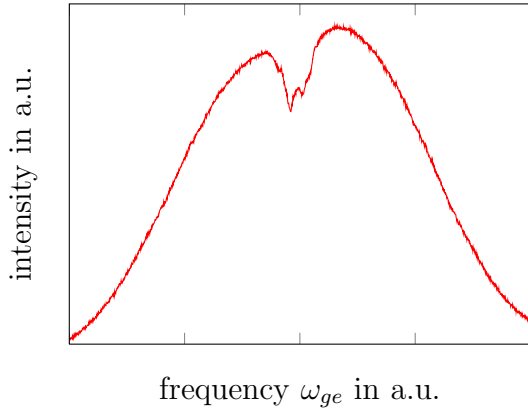
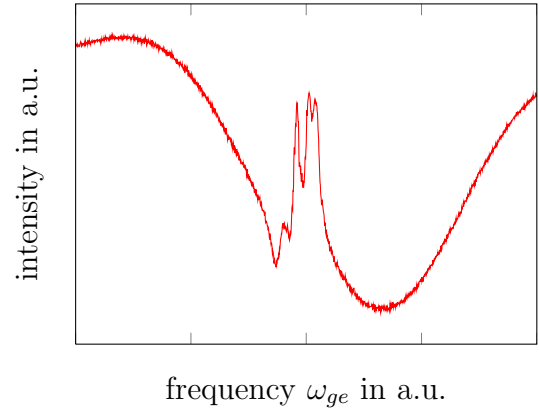


Figure 3.3.: The solid black lines show the level scheme of the ground state transitions of  $^{85}\text{Rb}$  in a magnetic field. Dashed lines correspond to the levels without Zeeman splitting. Each one of the orange and violet arrows has the same length causing the shifted absorption spectra for  $\sigma^+$  and  $\sigma^-$  light in the Dichroic Atomic Vapor Laser Lock. The transition  $5S_{1/2} \ F = 2 \rightarrow 5P_{3/2} \ F' = 3$  is shown.



(a) Absorption of the 780 nm beam for a  $\sigma$  component plotted against the frequency of the 780 nm laser.



(b) DAVLL lock signal: difference of the absorption of the  $\sigma$  components plotted against the frequency of the 780 nm laser.

Figure 3.4.: Absorption and DAVLL lock signal

## 3.2. EIT spectroscopy

The second laser, which is used as the seed laser for the Rydberg transition (480 nm), is locked via EIT spectroscopy. In order to choose the frequency and stabilize the laser for the upper excitation, both lasers are overlapped inside a rubidium cell whereas the blue laser passes the cell twice in co- and counter-propagating direction as shown in figure 3.5. The influence of the Doppler effect is outlined in figure 3.6. Let us assume the 780 nm laser is detuned from resonance by a certain detuning  $\delta_{ge}$ . This detuning can be compensated by a Doppler shift with a velocity  $v$  of an atom of

$$v = \frac{c \cdot \delta_{ge}}{\Delta_{ge}}. \quad (3.1)$$

For a co-propagating configuration, the energy level of the Rydberg state shifts in the same direction and hence the total detuning increases as illustrated in figure 3.6a. In counter-propagating direction the velocity in respect to the Rydberg laser is reversed and the frequency shift is overcompensated because the Doppler detuning depends on the transition frequency ( $\Delta_{er} > \Delta_{ge}$ ) as illustrated in figure 3.6b. Thus two signals arise, one of the co- and one of the counter-propagating laser, which are plotted in figure 3.7a. The distance  $\delta_{cc}$  of the two resonances results in

$$|\delta_{cc}| = 2 |\delta_{er,v}| = 2 |\delta_{ge,v}| \frac{\Delta_{er}}{\Delta_{ge}}. \quad (3.2)$$

As for the DAVLL lock, a zero crossing signal is required to stabilize the laser. Hence the same scheme with the Zeeman shift (compare figure 3.3) is used to create a lock signal out of the  $\sigma^+$  and  $\sigma^-$  components, which is shown in figure 3.7b. The signal can also be used as frequency reference according to equation (3.2). More details on the EIT with DAVLL can be found for example in [27].

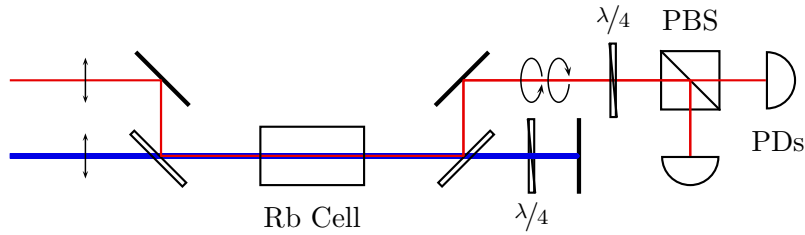


Figure 3.5.: EIT spectroscopy for 480 nm laser lock

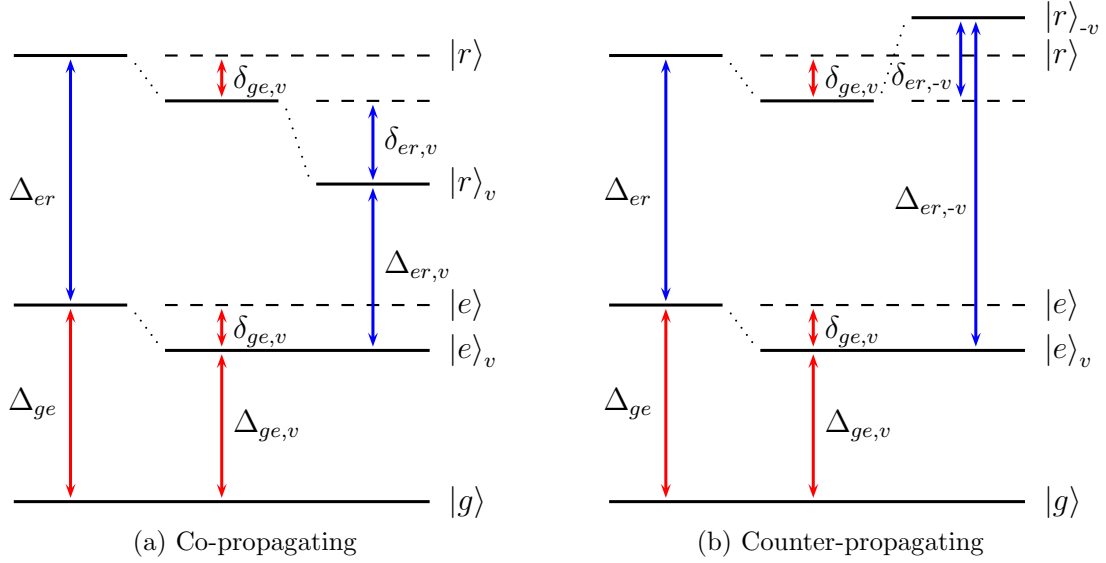


Figure 3.6.: Doppler effect leads to a detuning from resonance. Diagram shows co- and counter-propagating Doppler shift for a velocity class  $v < 0$  with detuning  $\delta_{ge,v}$ . In each figure the left part shows the energy levels for an atom at rest, in the center the level shift of the  $ge$ -transition is taken into account and on the right the shift of the  $er$ -transition is added.

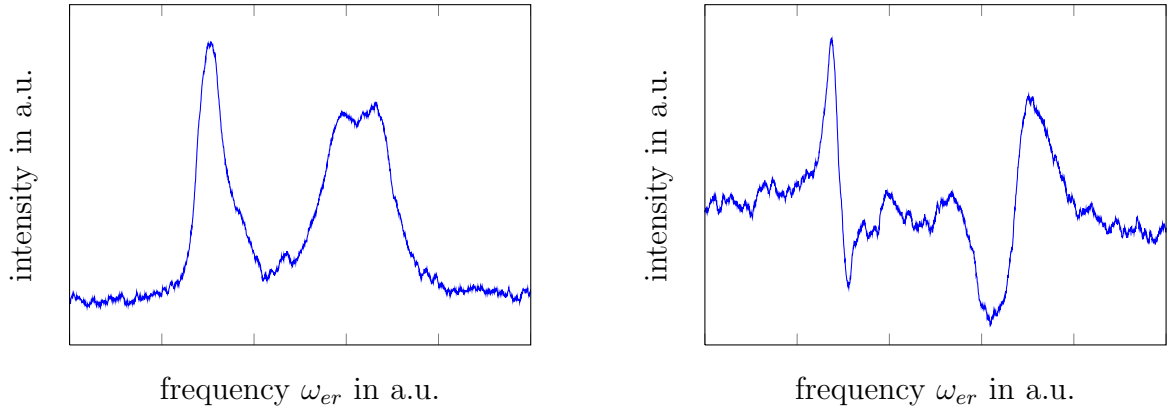


Figure 3.7.: EIT and EIT lock signal



### 3.3. Pulsed laser setup

The experiment requires Rabi frequencies of at least a few hundred MHz for both transitions in the three-level system, so that coherent effects can be observed in respect to the decay rate. The Rabi frequency

$$\Omega = -\frac{d_{12}E_0}{\hbar}$$

is proportional to the amplitude of the light field  $E_0$  and the corresponding dipole matrix element  $d_{12}$ , as introduced in section 2.2.2. The dipole matrix element for a transition between the excited and the Rydberg state ( $5P_{3/2} F = 3$  to  $30S_{1/2}$ ) is  $d_{er} = 1.2 \cdot 10^{-31}$  Cm [11, 28] for  $^{85}\text{Rb}$ . This is extremely small compared to the matrix element for the transition between the ground and the excited state ( $5S_{1/2} F = 2$  to  $5P_{3/2} F' = 3$ )  $d_{ge} = 1.09 \cdot 10^{-29}$  Cm [28, 29] for  $^{85}\text{Rb}$  and  $^{87}\text{Rb}$ . Therefore we need a high intensity of the 480 nm laser. This is realized with a pulsed laser setup that amplifies the 480 nm laser light. Similar amplification systems are described in [30] and [31].

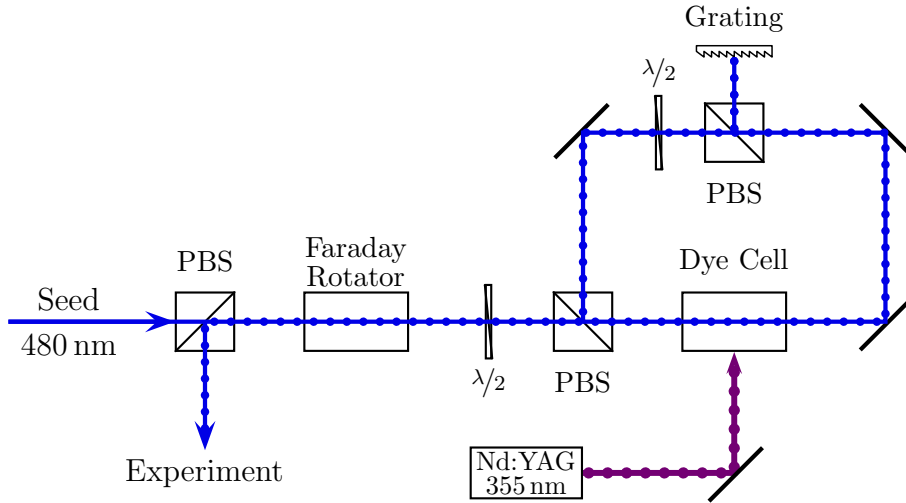


Figure 3.8.: The pulsed laser setup consists of a dye cell pumped by a frequency tripled pulsed YAG. The cell is seeded by the 480 nm beam in four pass configuration.

The pulsed laser setup is shown in figure 3.8. It contains a dye cell, which is pumped by a pulsed frequency-tripled YAG-laser of 355 nm. The 480 nm seed laser passes the cell four times. Due to the excited molecules of the dye, stimulated emission leads to amplification of the 480 nm seed light. Note that a four pass configuration with a single dye cell is the highest number of passes with exactly the same trajectory possible: the beam in the first and the second pass is specified by its polarization, in the third and the fourth pass it is

### 3. *Experimental setup*

---

distinguishable from the beam in the first and the second pass by its propagation direction. The pump laser is a frequency tripled 1064 nm YAG-laser Continuum Powerlite II 8050, which provides a time-averaged power up to 7 W of 355 nm light. The pulses have a repetition rate of 50 Hz and a full width at half maximum duration of about 6 ns.

The dye cell is made out of glass, containing a bore for the dye and the beam with a diameter of 1.6 mm. The 480 nm seed laser is guided through the bore of the cell, having about the same diameter in order to reach a high efficiency. The dye solution consists of 0.2 g Coumarin 102 dissolved in 1  $\ell$  ethanol. Amplified spontaneous emission results in unfavorable fluorescence light, which is suppressed by diffraction at a grating (for more details see [32]).

With this setup a pulse intensity of a few mJ per pulse can be reached. The pulse is Fourier-limited. More details and specifications of the system can be found in [33].

### 3.4. Setup for Rydberg excitation

For the experiment presented in this thesis, a 5 mm glass cell (see figure 3.9) is used. The cell contains a reservoir of rubidium, which can be heated to increase the atomic density inside as shown in figure 3.10. The cell itself is heated to a higher temperature than the reservoir in order to avoid condensation of rubidium atoms on the surface. The optical density and temperature of the rubidium vapor is determined by absorption spectroscopy.

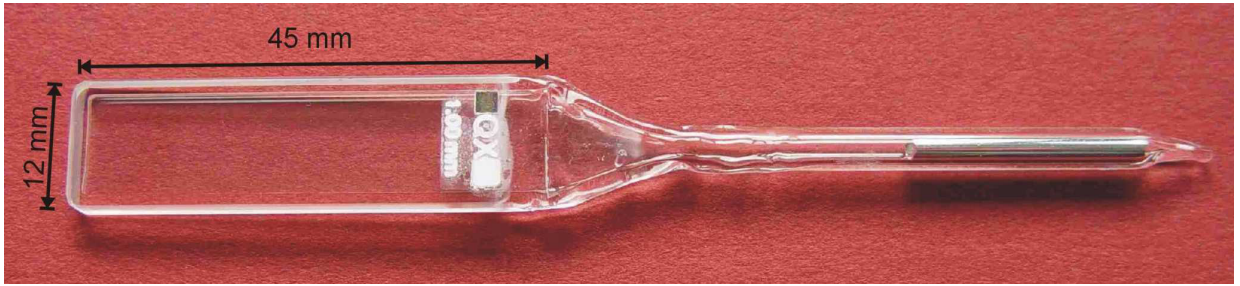


Figure 3.9.: Picture of a glass cell similar to the one used in the experiment. The cell contains a reservoir filled with rubidium.

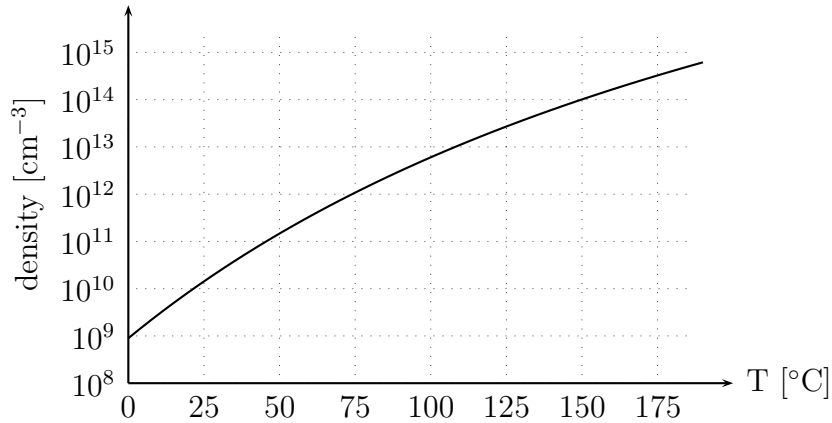


Figure 3.10.: Density of atomic rubidium at vapor pressure [28].

Inside the cell, the 780 nm beam and the 480 nm pulse are overlapped in almost counter-propagating configuration ( $\alpha = 171.5^\circ$ ; setup see figure 3.11). With a full counter-propagating setup the overlap at the surface of the cell leads to a dirt effect (observed signal dropping to zero). Nevertheless the angle must not be large in order to repress the Doppler broadening, which will be examined in section 5.2.3. The overlapping range of the two beams is approximately  $\Delta z = 2.5$  mm.

### 3. Experimental setup

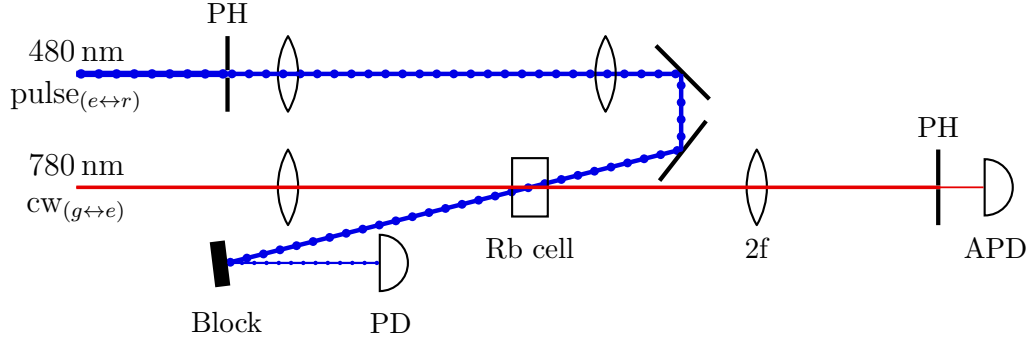


Figure 3.11.: Optical setup for the measurement. The 480 nm and 780 nm beams are overlapped inside the cell and both transmissions are recorded by photodiodes.

To observe Rabi oscillations, it is important to have a spatially constant intensity profile inside the interaction volume. Hence the 480 nm pulse ( $\varnothing \simeq 1300 \mu\text{m}$ ) is trimmed at an aperture ( $\varnothing = 575 \mu\text{m}$ ). This wavefront is imaged with two lenses into the rubidium cell ( $\varnothing \simeq 375 \mu\text{m}$ ) as captured in figure 3.12. Moreover, the 780 nm probe beam in the overlapping volume ( $1/e^2 \varnothing = 340 \mu\text{m}$ ) is imaged with a  $2f$  imaging onto an aperture ( $\varnothing = 150 \mu\text{m}$ ) directly in front of the probe APD to cut out the inner part as illustrated in figure 3.13.

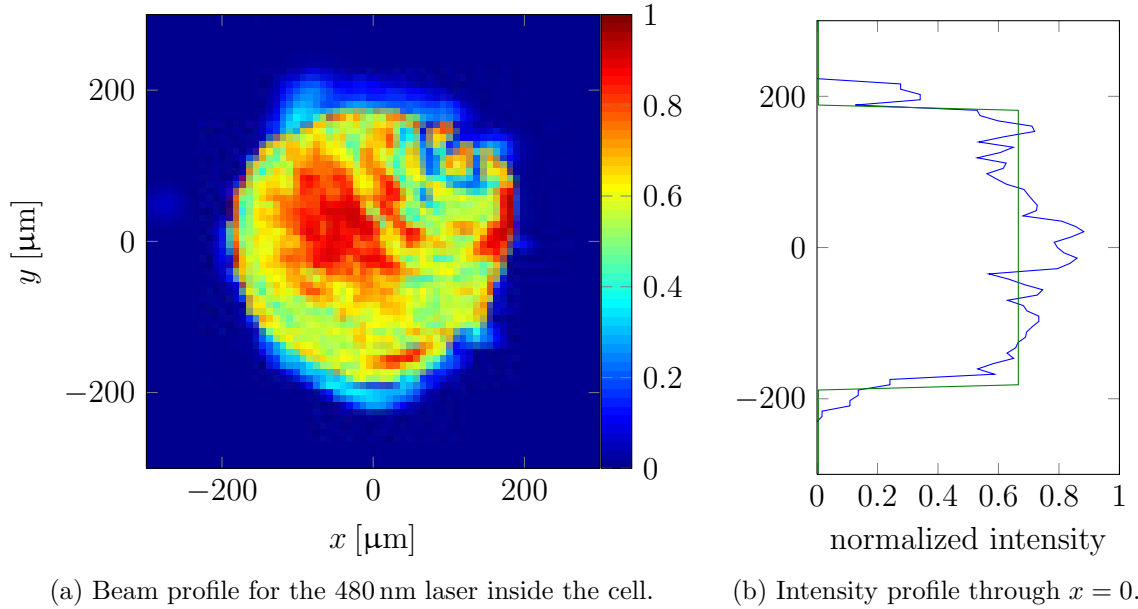
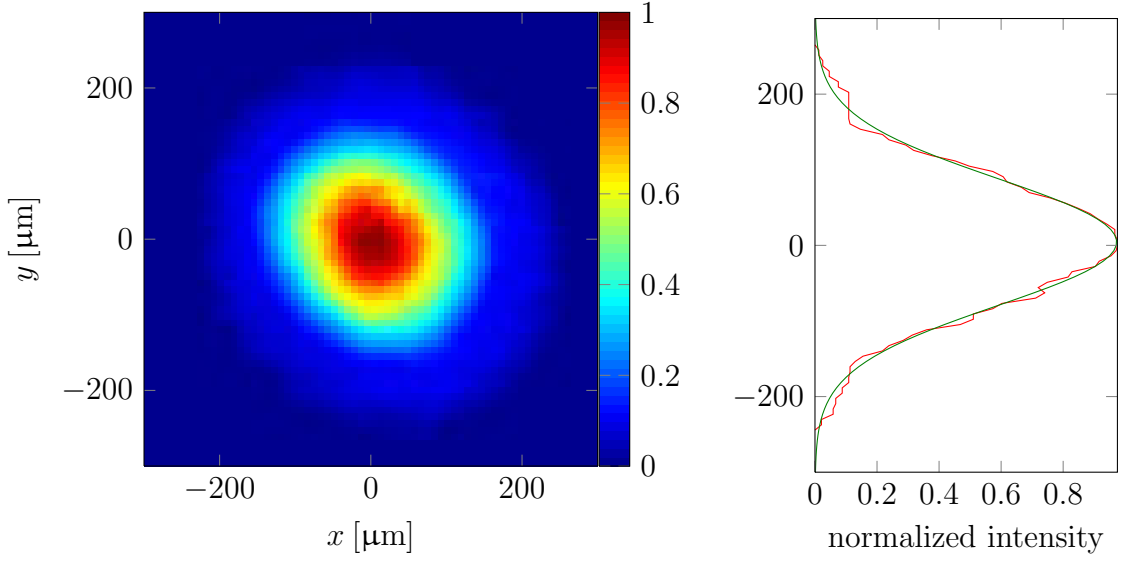


Figure 3.12.: Beam characteristics of the 480 nm light inside the cell, showing an almost rectangular intensity profile with a diameter of  $\sim 375 \mu\text{m}$ .



(a) Beam profile for the 780 nm laser inside the cell. (b) Intensity profile through  $x = 0$ .

Figure 3.13.: Beam characteristics of the 780 nm light inside the cell with a  $1/e^2$  diameter of 340  $\mu\text{m}$ .

In order to correlate the occurring oscillations of the lower transition to the pulse intensity the temporal pulse shape has to be known. After passing the cell the pulse is scattered on a white surface to reduce its intensity. The stray light is detected on a photodiode (EOT ET-2000) to record the temporal pulse shape. A comparison of the detection characteristics of different photodiodes is shown in figure 3.14. The experimental data is taken with an oscilloscope (LeCroy WaveSurfer 104MXs) at a sampling rate of 5 GS/s.

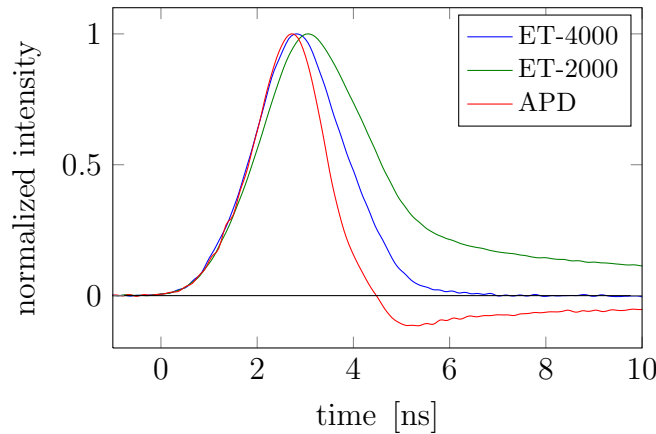


Figure 3.14.: Comparison of the detection characteristics of different photodiodes. The ET-4000 shows to most realistic pulse shape since the electrical characteristics suit well to the requirements. For the ET-2000 the falling slope is too slow, the APD suffers from AC coupling.

## 4. Experimental results

For the first time it was possible to show Rabi oscillations to a Rydberg state on the gigahertz scale. The data presented here is in good agreement with the three-level system introduced in section 2.2.3. The model to describe the experiment is surprisingly simple in respect to the complex level structure of an atom. Even though it is simple, the data shows a range of interesting features which will be discussed in detail.

Three related measurements are performed building one data set:

- absorption spectrum (scan of  $\delta_{ge}$ ) at low intensity ( $I_{ge} < I_{ge,sat}$ ) to determine the optical density, the atomic density and the temperature inside the cell with disabled pulsed laser ( $I_{er} = 0$ )
- blue intensity scan ( $I_{er}$ ) on resonance ( $\delta_{ge} = 0$ ,  $\delta_{er} = 0$ ) with constant intensity ( $I_{ge} = \text{const}$ ) for the lower transition
- blue frequency scan ( $\delta_{er}$ ) at fixed pulse intensity ( $I_{er} = \text{const}$ ) with the red laser being on resonance ( $\delta_{ge} = 0$ ) with constant intensity ( $I_{ge} = \text{const}$ )

At first, an overview over the measured data is given. The detailed discussion will follow in chapter 5.

### 4.1. Experimental parameters

The optical density, the atomic density and the temperature inside the cell are three basic parameters of the experiment. In order to determine these values an absorption spectrum is taken by the probe laser at low intensity ( $I_{ge} < I_{ge,sat}$ ). A fit function containing the required parameters is fitted to the signal as shown in figure 4.1. On resonance the signal drops to zero because of the high optical density inside the 5 mm glass cell. The values extracted from the fit are a temperature of  $T = 120$  °C, an atomic density of  $n_{\text{cell}} = 4.5 \cdot 10^{12} \text{ cm}^{-3}$  and an optical density of  $\sim 21$  for the transition  $^{85}\text{Rb } 5S_{1/2} F = 2$

to  $5P_{3/2}$ , which is later used to excite the atoms from the ground state to the intermediate state. For the transition to the Rydberg state the optical density is low due to the low dipole matrix element of the Rydberg transition. Hence effects like pulse propagation or self-induced transparency can be neglected.

The effective density of atoms which are involved in the excitation scheme is less than the total density  $n_{\text{cell}}$  due to the natural isotope ratio of rubidium ( $^{85}\text{Rb}$ : 72 %). As a second loss the hyperfine ratio of the driven ground state transition  $^{85}\text{Rb } 5S_{1/2} F=2$  to  $5P_{3/2}$  (see section 5) with ratio of 5/12 reduces the addressable atoms. Hence the effective density has come to  $n = 1.3 \cdot 10^{12} \text{ cm}^{-3}$  in the given setup.

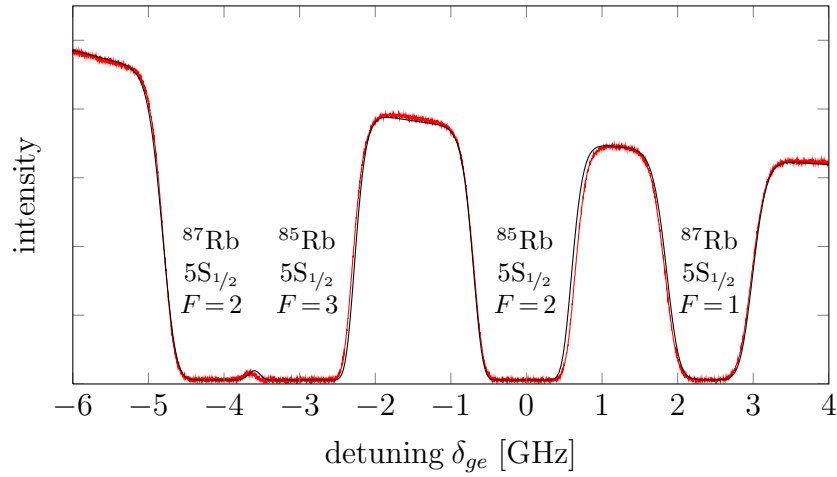


Figure 4.1.: Absorption spectrum of the D<sub>2</sub>-line to determine the optical density and temperature inside the cell. The red signal shows the measured data, the black line the fit function used to extract the parameters.  $\delta_{ge} = 0$  marks the center of the Doppler valley of the transition  $^{85}\text{Rb } 5S_{1/2} F=2$  to  $5P_{3/2}$  used in the experiment.

## 4.2. Rabi oscillations

As described in section 3.4, the oscillations in the absorption appear as soon as the upper excitation is driven by the pulsed laser. In figure 4.2 Rabi oscillations are shown from a single shot experiment. In the steady state ( $t < 0$ ) the observed signal on the APD is zero since the photodiode is ac coupled. At  $t = 0$  the blue pulse arrives and oscillations appear in the probe field, due to the changing coherences. The peak pulse intensity is measured as  $I_{er} \simeq 22 \text{ MW/cm}^2$ . Already in this single event it can be seen that the oscillation frequency depends on the temporal evolution of the blue intensity. During the pulse, the oscillation frequency starts slow at the beginning, increases and slows down again. After the pulse at about 5.5 ns, the system is not in equilibrium anymore and damped oscillations show the relaxation into the steady state. The frequency of this oscillation gives access to the Rabi frequency of the lower transition ( $\Omega_{ge} \simeq 2\pi \cdot 200 \text{ MHz}$ ). With the corresponding dipole matrix element (see section 3.3) an electric field of  $E_{ge} = 1.2 \cdot 10^4 \text{ V/m}$  and an intensity of  $I_{ge} = 2.0 \cdot 10^5 \text{ W/m}^2$  are calculated for this transition.

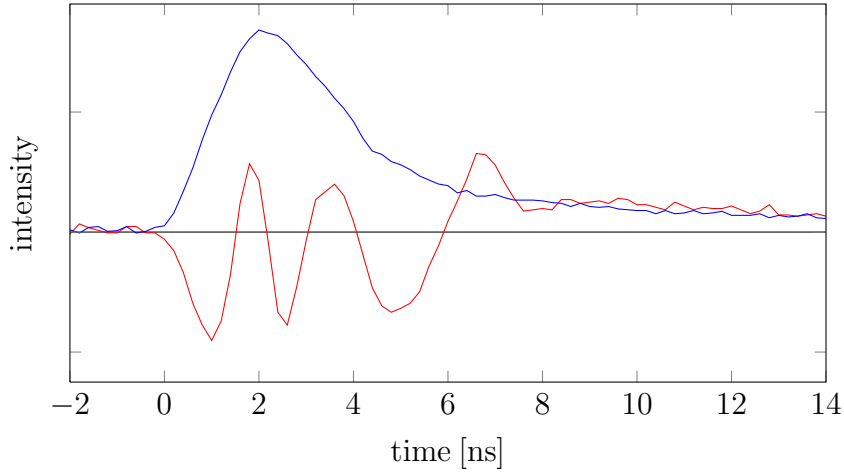


Figure 4.2.: Single shot data: the blue line shows the pulse for the Rydberg excitation and the red line the emerging Rabi oscillations of the probe beam (amplitudes are not to scale). After the pulse the system is evolving back into steady state. The falling slope of the pulse is actually steeper than shown here. This is due to the characteristics of the photodiode used here (see figure 3.14, ET-2000).



### 4.2.1. Rabi oscillations for different pulse intensities

By changing the intensity of the pulse  $I_{er}$ , the effective Rabi oscillation changes. According to the theory for both transitions on resonance ( $\delta_{ge} = 0$ ,  $\delta_{er} = 0$ )

$$\Omega'_{er} = \sqrt{\Omega_{ge}^2 + \Omega_{er}^2} \quad [33] \quad (4.1)$$

$$\Omega_{er} = \frac{d_{er} E_{0,er}}{\hbar} \quad (4.2)$$

$$I_{er} = \frac{1}{2} c \epsilon_0 E_{0,er}^2, \quad (4.3)$$

where  $I_{er}$  is the intensity of the upper transition,  $d_{er}$  the dipole matrix element and  $E_{0,er}$  the amplitude of the electric field, the effective Rabi frequency  $\Omega'_{er}$  shows a square root like behavior

$$\Omega'_{er} = \sqrt{\Omega_{ge}^2 + \text{const} \cdot I_{er}^2}. \quad (4.4)$$

The experimental and simulated data are presented in figure 4.3 which are in good agreement. The pulse intensity increases from left to right and therefore the oscillation frequency increases likewise.

### 4.2.2. Rabi oscillations for different pulse detunings

For the third measurement the peak pulse intensity of the upper laser to the Rydberg state is held constant ( $I_{er} \simeq 22 \text{ MW/cm}^2$ ), while its detuning  $\delta_{er}$  is scanned. The lower transition is on resonance ( $\delta_{ge} = 0$ ). The experimental data and the corresponding simulation can be seen in figure 4.4. For a two-level system one would expect faster oscillations out of resonance ( $|\delta_{er}| > 0$ ) because of  $\Omega'_{er} = \sqrt{\Omega_{er}^2 + \delta_{er}^2}$  (see equation 2.26). However, the experiment and simulation show a decreasing oscillation frequency with increasing detuning instead.

In order to explain this behavior a detailed discussion will be shown in the next chapter.

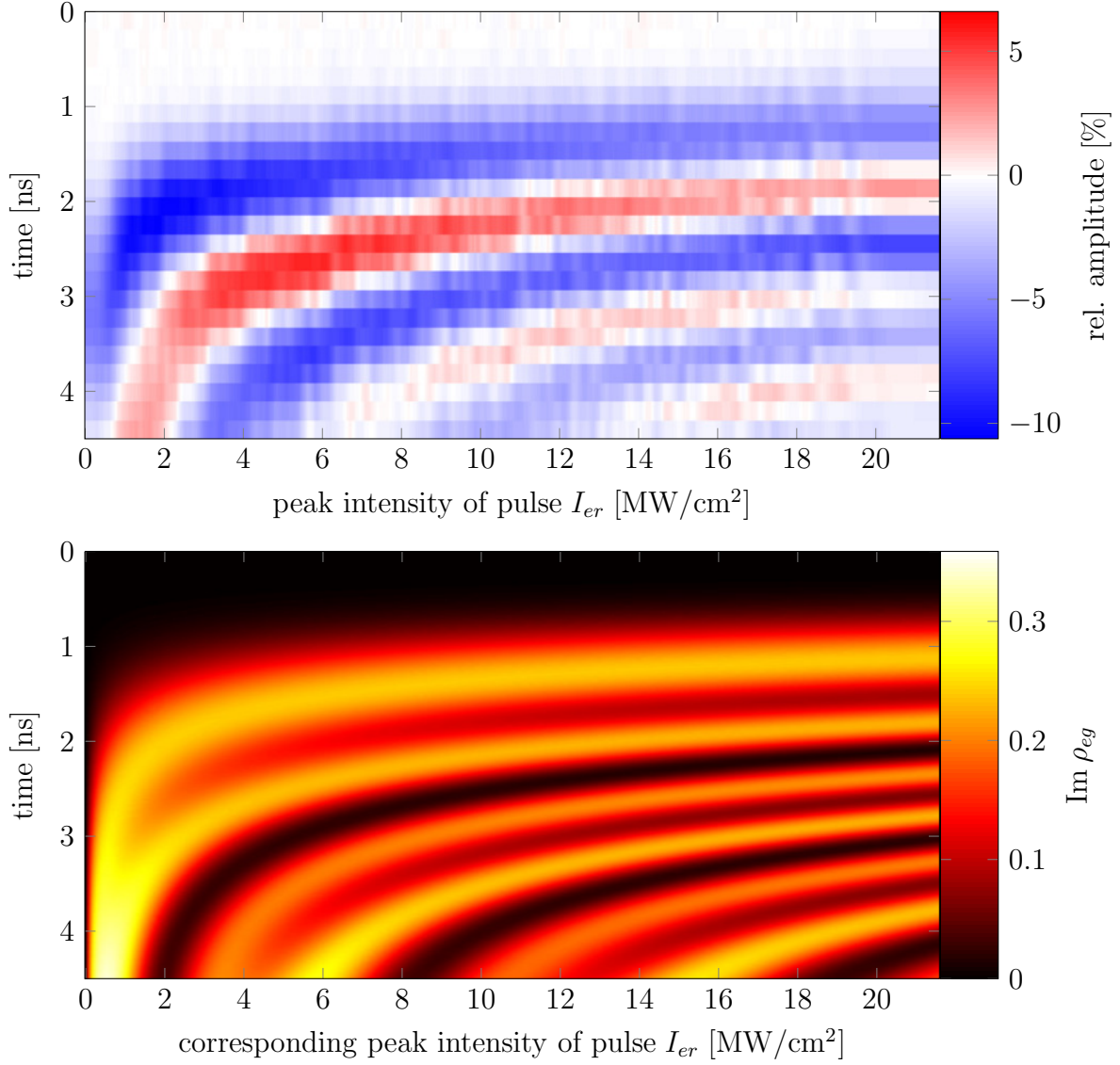


Figure 4.3.: Experimental data (upper picture) of an intensity scan  $I_{er}$  of the upper transition with a peak pulse intensity of up to  $\sim 22$  MW/cm<sup>2</sup>. For the simulation (lower picture) the peak Rabi frequency is chosen to be  $\Omega_{er} = 2\pi \cdot 2.2$  GHz to best fit the experiment.

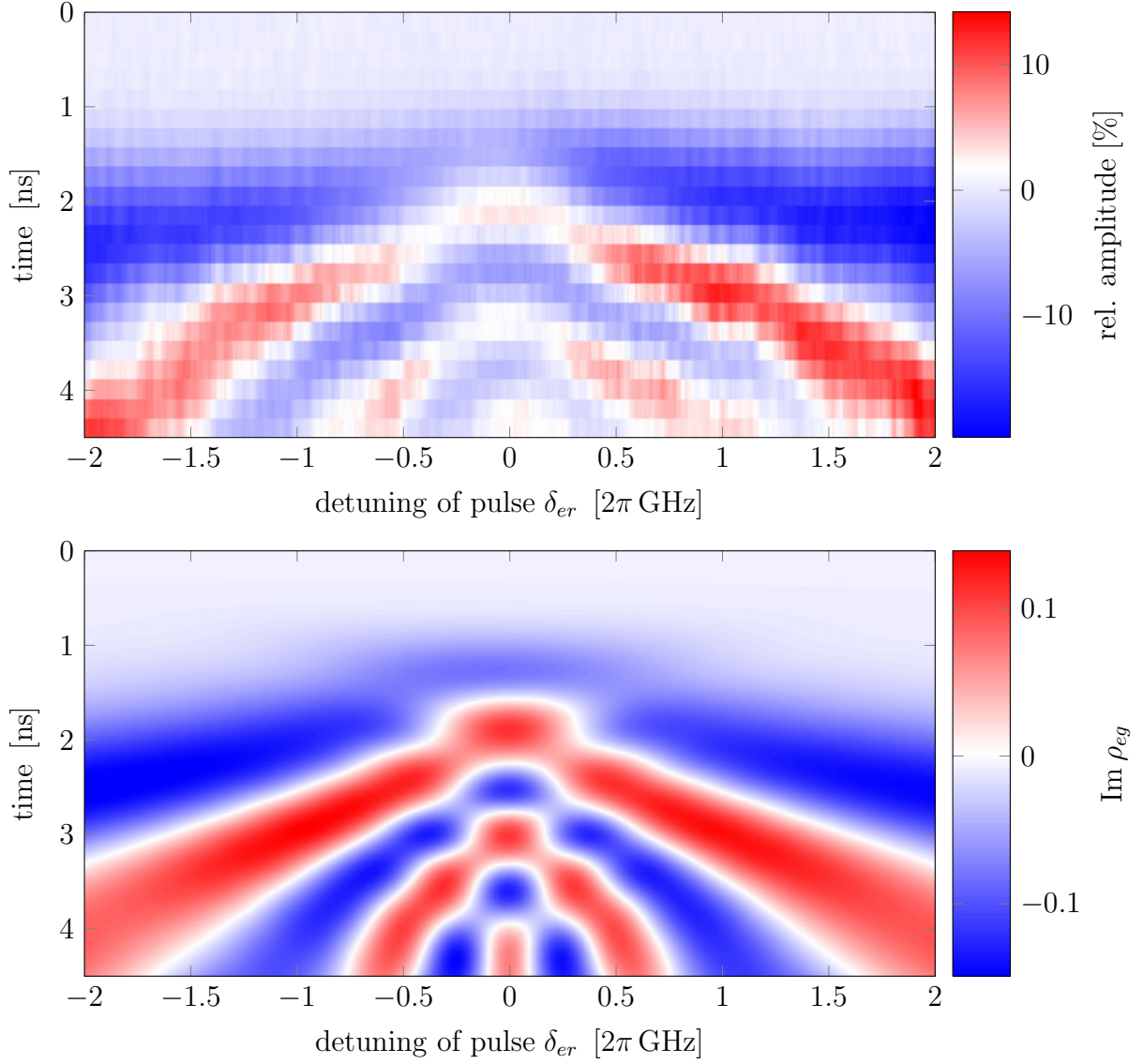


Figure 4.4.: Experimental data (upper picture) of a detuning scan  $\delta_{er}$  with a peak pulse intensity of  $I_{er} \simeq 22 \text{ MW/cm}^2$  and the corresponding simulation (lower picture) with a peak Rabi frequency of  $\Omega_{er} = 2\pi \cdot 2 \text{ GHz}$  chosen to best fit the experiment.

## 5. Simulation and discussion

The simple model of a three-level system (see section 2.2.3) is capable of describing the features of this experiment. Even though rubidium is used, it turns out that the whole level scheme can be reduced to a ground state, an excited state and a Rydberg state which will be shown in the next paragraph. This basic model can be simulated easily and allows for a separated analysis of the occurring effects in order to give an intuitive picture for the interpretation of the experimental data.

So why can we simplify the level scheme? For rubidium as an alkali atom the lower excitation from the ground to the excited state can be realized by the D<sub>1</sub> transition 5S<sub>1/2</sub> to 5P<sub>1/2</sub> or the D<sub>2</sub> line 5S<sub>1/2</sub> to 5P<sub>3/2</sub> which are well separated in rubidium with  $\sim 7.1$  THz. The ground state transitions including the hyperfine structure are illustrated in appendix A. The hyperfine splitting of the ground state is  $\sim 3.0$  GHz for <sup>85</sup>Rb and  $\sim 6.8$  GHz for <sup>87</sup>Rb which both exceed the Doppler broadening at  $T = 120$  °C of  $\delta_{ge,\text{FWHM}} \simeq 0.5$  GHz and hence can be resolved. The ground state used in the experiment is <sup>85</sup>Rb 5S<sub>1/2</sub>  $F = 2$ . The addressable hyperfine levels from the ground state at  $F = 2$  to the excited state cannot be resolved since the frequency range from <sup>85</sup>Rb 5P<sub>3/2</sub>  $F' = 1$  to  $F' = 3$  is only 93 MHz. They are treated as one due to the Doppler broadening and the bandwidth of the upper excitation which is  $\sim 2$  GHz caused by the high intensities used ( $I_{er} \simeq 22$  MW/cm<sup>2</sup>  $\hat{=}$   $\Omega_{er} \simeq 2$  GHz). Also the transitions of the isotope <sup>87</sup>Rb are well separated from <sup>85</sup>Rb and thus do not contribute. The Rydberg state 30S<sub>1/2</sub> is also well separated from other states whereas the hyperfine structure is not resolved. This allows for reducing the system to a simple three-level model. The coupling between the states is given by two light fields: the so-called probe laser for the lower transition and the coupling laser for the upper transition.

Here a short summary of the simulation model is given. The density matrix is defined by

$$\rho(t) := \begin{pmatrix} \rho_{gg}(t) & \rho_{ge}(t) & \rho_{gr}(t) \\ \rho_{eg}(t) & \rho_{ee}(t) & \rho_{er}(t) \\ \rho_{rg}(t) & \rho_{re}(t) & \rho_{rr}(t) \end{pmatrix}. \quad (5.1)$$

The dynamic of the system is described by the Liouville-von Neumann equation

$$\frac{\partial \rho}{\partial t} = -\frac{i}{\hbar}[H, \rho] + \mathcal{L}_D(\rho) \quad (5.2)$$

and the corresponding Hamilton operator for this system in the rotating wave approximation is given by

$$H(t) = \begin{pmatrix} 0 & \frac{1}{2}\Omega_{ge}(t) & 0 \\ \frac{1}{2}\Omega_{ge}(t) & -\delta_{ge} & \frac{1}{2}\Omega_{er}(t) \\ 0 & \frac{1}{2}\Omega_{er}(t) & -\delta_{ge} - \delta_{er} \end{pmatrix}. \quad (5.3)$$

The Lindblad operator which includes two decay channels  $\Gamma_{re}$  and  $\Gamma_{eg}$  results in

$$\mathcal{L}_D(t) = \begin{pmatrix} \Gamma_{eg}\rho_{ee}(t) & -\frac{1}{2}\Gamma_{eg}\rho_{ge}(t) & -\frac{1}{2}\Gamma_{re}\rho_{gr}(t) \\ -\frac{1}{2}\Gamma_{eg}\rho_{eg}(t) & -\Gamma_{eg}\rho_{ee}(t) + \Gamma_{re}\rho_{rr}(t) & -\frac{1}{2}\Gamma_{eg}\rho_{er}(t) - \frac{1}{2}\Gamma_{re}\rho_{er}(t) \\ -\frac{1}{2}\Gamma_{re}\rho_{rg}(t) & -\frac{1}{2}\Gamma_{eg}\rho_{re}(t) - \frac{1}{2}\Gamma_{re}\rho_{re}(t) & -\Gamma_{re}\rho_{rr}(t) \end{pmatrix}. \quad (5.4)$$

The initial steady state  $\Omega_{ge} = \text{const}$ ,  $\Omega_{er} = 0$  is calculated to be

$$\rho(0) = \begin{pmatrix} 1 - \frac{\Omega_{ge}^2}{4\delta_{ge}^2 + \Gamma_{eg}^2 + 2\Omega_{ge}^2} & \frac{2\Omega_{ge}(\delta_{ge} - i\Gamma_{re}/2)}{4\delta_{ge}^2 + \Gamma_{eg}^2 + 2\Omega_{ge}^2} & 0 \\ \frac{2\Omega_{ge}(\delta_{ge} + i\Gamma_{re}/2)}{4\delta_{ge}^2 + \Gamma_{eg}^2 + 2\Omega_{ge}^2} & \frac{\Omega_{ge}^2}{4\delta_{ge}^2 + \Gamma_{eg}^2 + 2\Omega_{ge}^2} & 0 \\ 0 & 0 & 0 \end{pmatrix}. \quad (5.5)$$

The ordinary differential equation (5.2) was solved numerically with a Runge-Kutta method (RK4) in *Mathematica* and to speed up the calculations in a native *Java* program (more details can be found in appendix B.1). An integration time step of  $\Delta_t = 0.1$  ns is chosen to sample the results sufficiently accurate. The simulation parameters are the following:

decay rate $r \rightarrow e$	$\Gamma_{re}$	10 kHz
decay rate $e \rightarrow g$	$\Gamma_{eg}$	6 MHz
Rabi frequency $g \leftrightarrow e$	$\Omega_{ge}$	$2\pi \cdot 200$ MHz
time step	$\Delta t$	0.1 ns
temperature	$T$	120 °C
crossing angle of beams	$\alpha$	171.5 °

The dynamics of the system are driven by the time dependent pulse intensity and hence the Rabi frequency  $\Omega_{ge}(t)$ . For a thermal gas, the Doppler velocities have to be taken into account. Hence, the simulation is performed for  $N = 1000$  atoms where the velocity of each atom has a random value according to the Maxwell-Boltzmann distribution.

For an experimental setup where both beams are in full counter-propagation direction ( $\alpha = 180^\circ$ ), only one dimension of the velocity distribution is required:

$$p(v) = \sqrt{\frac{m}{2\pi k_B T}} \exp\left(-\frac{mv^2}{2k_B T}\right). \quad (5.6)$$

The Doppler detuning  $\delta_v$  is calculated by

$$\delta_v = \omega_0 \frac{v}{c} \quad (5.7)$$

$$\delta'_{ge} = \delta_{ge} + \delta_{v,ge} \quad (5.8)$$

$$\delta'_{er} = \delta_{er} + \delta_{v,er}. \quad (5.9)$$

Note that the frequency shift for both light fields is not equal:

$$\frac{\delta_{v,er}}{\delta_{v,ge}} = -\frac{\lambda_{ge}}{\lambda_{er}} \approx -1.63 \quad (5.10)$$

The final density matrix is calculated by

$$\bar{\rho} = \frac{1}{N} \sum_{n=1}^N \rho_n, \quad (5.11)$$

where each  $\rho_n$  is the density matrix of the  $n$ -th simulation with a random velocity according to its probability (see equation 5.6). This formula, which is easily implemented in a simulation, converges to the analytical result

$$\rho = \int_v p(v) \rho(v) dv, \quad (5.12)$$

where  $p(v)$  is the Maxwell-Boltzmann distribution and  $\rho(v)$  the density matrix for a velocity  $v$ .

If the setup is neither co- nor counter-propagating, it is necessary to use a two dimensional velocity distribution, which is a simple extension to the given model. In the real experiment the crossing angle is  $\alpha = 171.5^\circ$ . The small difference to the counter-propagating configuration is almost negligible. The angular dependence will be discussed in section 5.2.3.

## 5.1. Rabi oscillations for different pulse intensities

As described in section 4.2.1, the simulation for different pulse intensities is in good agreement with the experiment (see figure 4.3). Whereas in the experiment the only accessible property is the absorption, the simulation also gives access to the population of the different states ( $\rho_{gg}$ ,  $\rho_{ee}$  and  $\rho_{rr}$ ) which are shown in figure 5.1. A peak pulse Rabi frequency of  $\Omega_{er} \simeq 2\pi \cdot 2.2$  GHz fits best the experimental data with a measured peak pulse intensity of  $I_{er} \simeq 22$  MW/cm<sup>2</sup>. The corresponding Rabi frequency calculated with the dipole matrix element of section 3.3 for the given intensity  $I_{er}$  would result in  $\Omega_{er} = 2\pi \cdot 2.3$  GHz. The difference between the calculated and the simulated Rabi frequency is in the tolerance of an estimated error of the intensity ( $I_{er} : \pm 10\%$ ) and the uncertainty of choosing the Rabi frequency in the simulation ( $\Omega_{er} : \pm 2\pi \cdot 150$  MHz) best fitting to the experimental data.

During one single pulse, six full Rabi cycles can be observed (figure 5.1c). A peak effective Rabi frequency of about  $\Omega'_{er} \simeq 2\pi \cdot 2.27$  GHz is achieved, extracted from the oscillations of the simulation. The enhancement of the Rabi frequency  $\Omega'_{er} - \Omega_{er} = 2\pi \cdot 70$  MHz is caused by the Rabi frequency of the lower transition according to equation (4.1)  $\Omega'_{er} = \sqrt{\Omega_{er}^2 + \Omega_{ge}^2}$  and the Doppler detuning with respect to equation (2.26)  $\Omega'_{er} = \sqrt{\Omega_{er}^2 + \delta_{er}^2}$ . Both effects are on the  $2\pi \cdot 10$  MHz scale.

The simulation of the excited state (figure 5.1b) shows a steady state ( $t = 0$ ) population of 24 %. At zero temperature, the state would be populated by 50 % as  $\Omega_{ge} \gg \Gamma_{ge}$ . The reduced population is due to the Doppler distribution at  $T = 120$  °C ( $\delta_{ge,FWHM} = 513$  MHz). For the Rydberg state a population of 35 % (figure 5.1c) can be achieved. In order to get significantly higher Rydberg populations the transition between the ground and the excited state has to be pulsed, too. As a proof of principle, a simulation is calculated in which both excitation pulses arrive at the same time, have the same Rabi frequency  $\Omega_{ge}(t) = \Omega_{er}(t)$  and have a  $1/e^2$  pulse width of 0.33 ns. With this simple excitation scheme a Rydberg population of well over 90 % can be achieved even in the thermal regime (see figure 5.2).

## 5.2. Rabi oscillations for different pulse detunings

The experimental data for different pulse detunings as presented in section 4.2.2 and figure 4.4 shows the effect of a decreasing oscillation frequency with increasing detuning  $|\delta_{er}|$ . In order to understand this behavior, it is instructive to further simplify the system. In a first approach the pulse shape is assumed to be rectangular with a constant Rabi frequency. A corresponding simulated absorption profile is plotted in figure 5.3. To make this

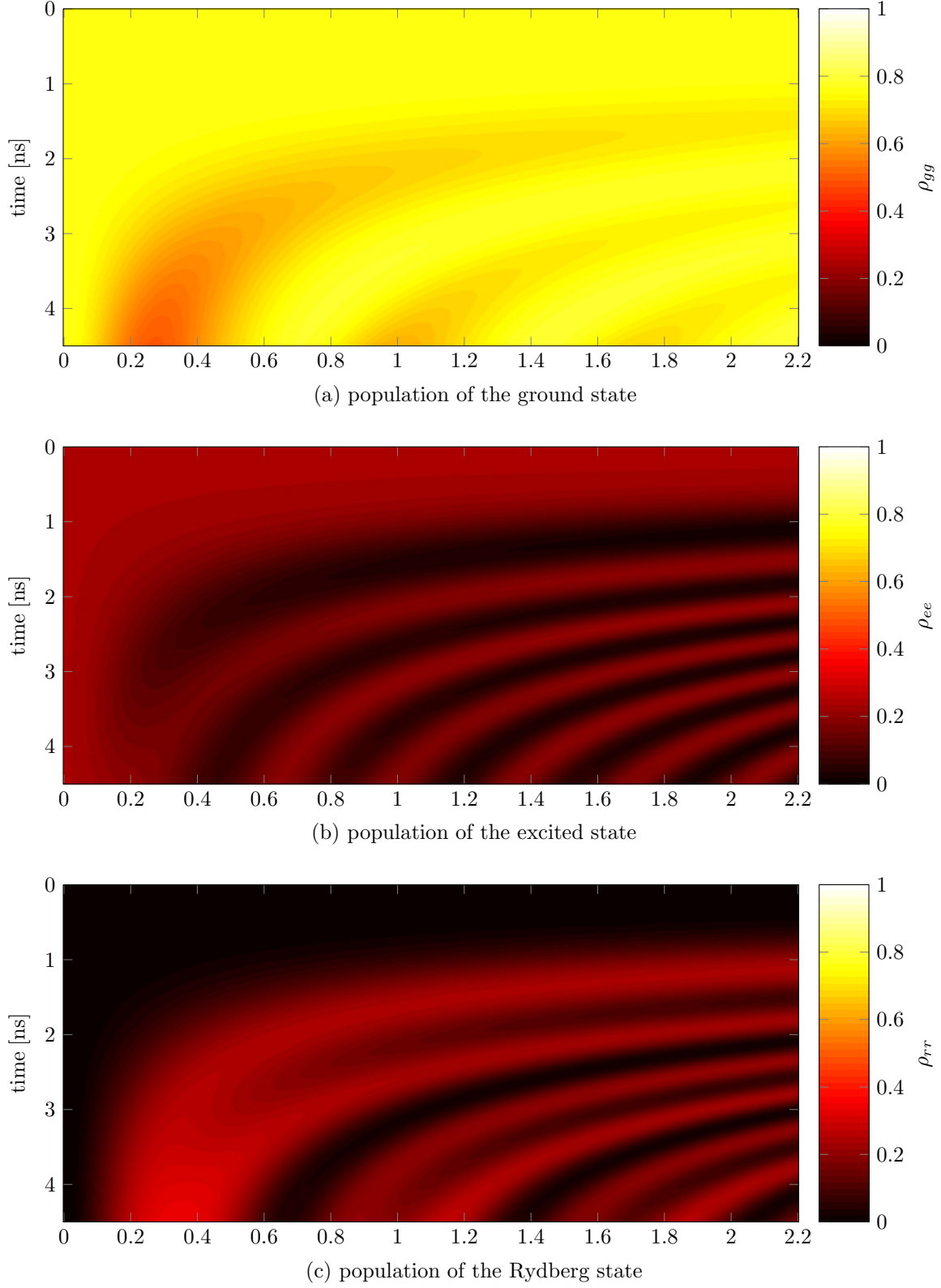


Figure 5.1.: Simulated population of each of the three levels.  
x-axis: pulse peak Rabi frequency  $\Omega_{er}$  in  $[2\pi \text{ GHz}]$



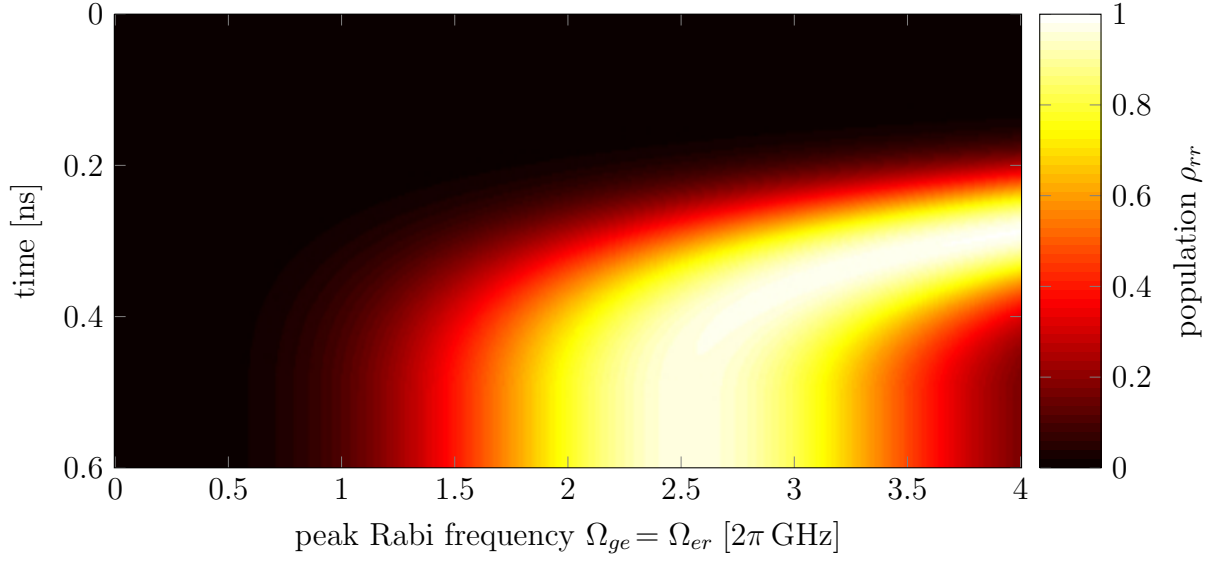


Figure 5.2.: Simulated population of the Rydberg state in a setup where both transitions are driven simultaneously with a  $1/e^2$  pulse width of 0.33 ns.

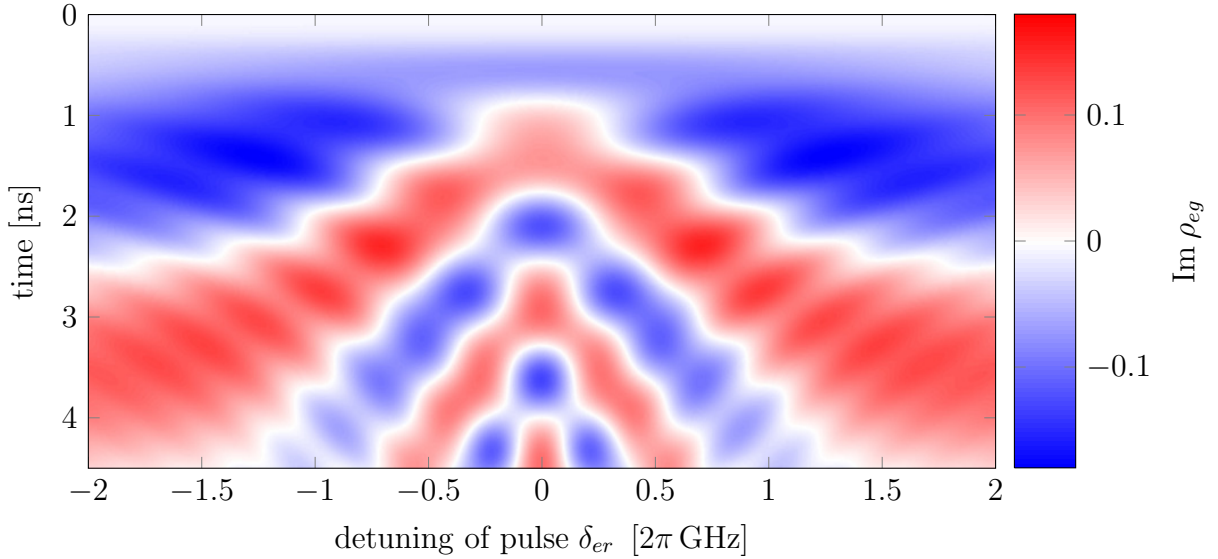


Figure 5.3.: Simulated absorption spectrum for a rectangular pulse shape with a constant Rabi frequency of  $\Omega_{er} = 2\pi \cdot 1.3$  GHz.

simulation comparable to the previous simulations the Rabi frequency for this simulation  $\Omega_{er} = 2\pi \cdot 1.3 \text{ GHz}$  is chosen such that the same number of oscillations occur in the first 4.5 ns, which is the plotted time range of most figures. The influence of the pulse shape will be examined in detail in section 5.2.2. First the Autler-Townes splitting in combination with the thermal velocity distribution is discussed which builds the framework for explaining the experimental data.

### 5.2.1. Autler-Townes splitting

The main properties of the experiment are described by an Autler-Townes splitting introduced in 2.2.4, involving the two upper states which is caused by the strongly driven upper transition with the pulsed laser. This coupled system is probed by the cw probe laser driving the lower transition. Since the Autler-Townes splitting and the Doppler shift have about the same magnitude, none of them dominates the system and the interplay of each other has to be examined.

The final density matrix of a simulation as given in equation (5.12) is the sum over all velocity dependent density matrices multiplied by their weight factor of the Maxwell-Boltzmann distribution. Hence a look at the different velocity classes is helpful for explaining the results of the system obtained. As a first velocity class we assume atoms at rest ( $v = 0$ ) so that no additional Doppler detuning occurs ( $\delta_{ge,v} = \delta_{er,-v} = 0$ ). The scan range for the detuning  $\delta_{er}$  we choose is within  $\pm 2\pi \cdot 2 \text{ GHz}$ . It is therefore symmetric with respect to  $\delta_{er} = 0$  and indicated by the blue line in the energy diagram in figure 5.4. The anticrossing point of the Autler-Townes splitting is exactly in the center of the absorption profile  $\delta_{er} = 0$ . For this velocity class the absolute absorption signal (figure 5.5) is weak because the levels of the dressed states cannot be crossed due to the anticrossing. At the center ( $\delta_{ge} = 0$ ) the two modes of the Autler-Townes doublet interfere constructively as they have a symmetric energy splitting of  $\pm \hbar \Omega_{er}/2$  at this frequency.

As a next velocity class we select a speed of  $-400 \text{ m/s}$  (figure 5.6). The Doppler shift causes a detuning of  $\delta_{ge,v} = -2\pi \cdot 513 \text{ MHz}$  and  $\delta_{er,-v} = 2\pi \cdot 829 \text{ MHz}$ . That means the probe range in the energy diagram has shifted to the right and slightly to the bottom due to the Doppler detuning (see figure 5.4). Here, one of the resonances of the dressed state is crossed and we observe a strong signal there (see figure 5.6) and the oscillation slows down according to  $\Omega'_{er} = \sqrt{\Omega_{er}^2 + \delta_{er}^2}$ . The absorption spectrum itself is not symmetric anymore but the sum over all velocities will end up being symmetric, since the absorption profiles of velocities  $v$  and  $-v$  are just flipped along the center of the frequency axis  $\delta_{er} = 0$ . In all plots the two modes arising from the Autler-Townes doublet are visible.

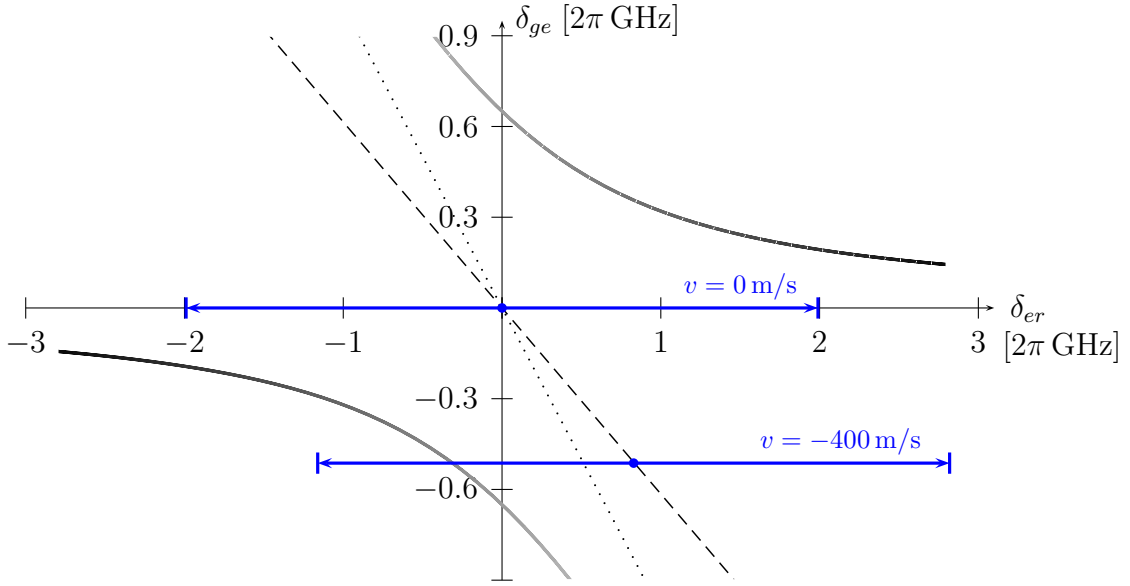


Figure 5.4.: Autler-Townes splitting for  $\Omega_{er} = 2\pi \cdot 1.3$  GHz. Frequency scans for  $v = 0$  m/s and  $v = -400$  m/s are highlighted in blue.

At the experimental temperature of  $T = 120$  °C the standard deviation of the velocity distribution is

$$\sigma_v = \sqrt{\frac{k_B T}{m}} = 196 \text{ m/s}. \quad (5.13)$$

A variety of velocity classes is shown in figure 5.7, where the color code indicates the simulated absorption strength multiplied by its weight factor according to the Maxwell-Boltzmann distribution (equation 5.6). Atoms at rest or with low velocity are far away from the resonances of the split system and hence have a low signal although their weight factor is high. At high velocities (e.g. 400 m/s) the signal is also low although a resonance is crossed because its weight factor has dropped to almost zero. Hence the velocities in between dominate the total absorption: at velocities of around  $|v| = 100$  m/s a resonance is almost inside the scan range and the corresponding weight factor is still high enough to give a strong signal. If we finally sum up all velocity classes, we end up with a simulated absorption profile (figure 5.3) close to the observed experimental signal (figure 4.4).

To conclude and explain the final result it can be said that the Autler-Townes doublet is probed by the different velocity classes that exist due to the Doppler distribution. The oscillations slow down with increasing scan detuning  $|\delta_{ge}|$  since both resonance frequencies of the Autler-Townes doublet are outside or at the edge of the scan range for the relevant velocity classes. In other words, the highest detuning from the Autler-Townes doublet is reached at  $\delta_{er} = 0$  and thus the oscillations are the fastest there.

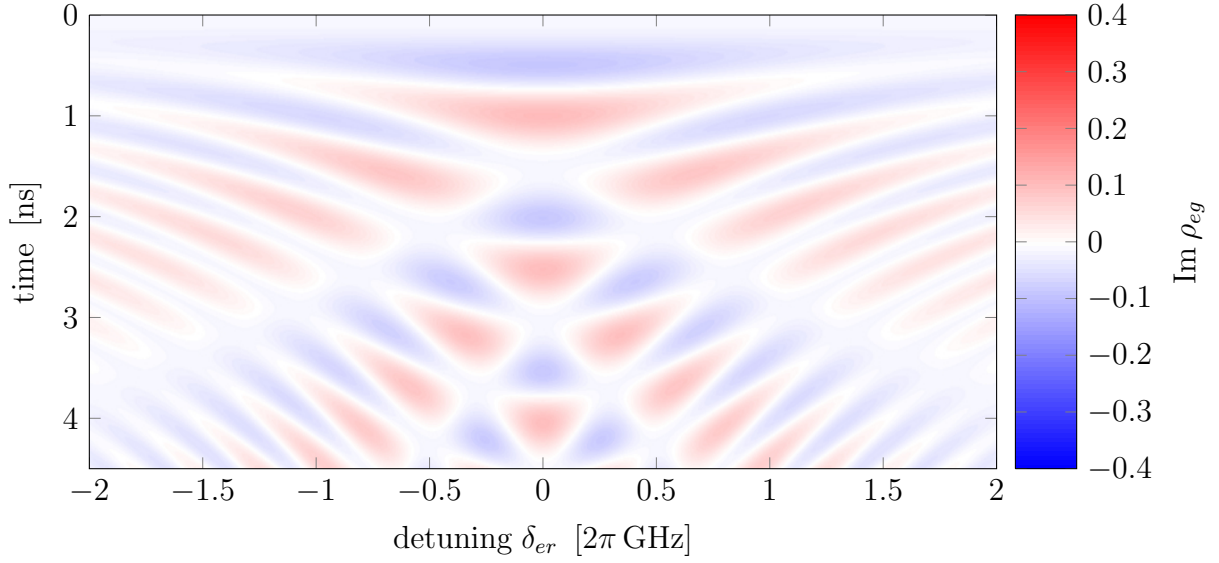


Figure 5.5.: Simulated absorption spectrum for the velocity class  $v = 0$  with a rectangular pulse shape of  $\Omega_{er} = 2\pi \cdot 1.3$  GHz.

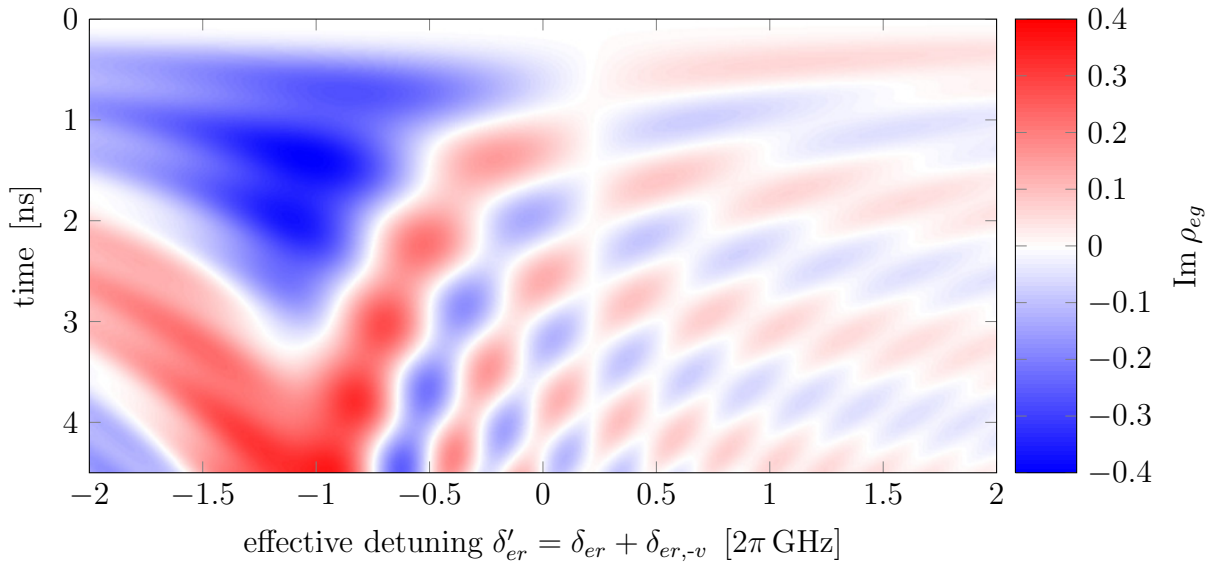


Figure 5.6.: Simulated absorption spectrum for the velocity class  $v = -400$  m/s with a rectangular pulse shape with  $\Omega_{er} = 2\pi \cdot 1.3$  GHz. The detunings resulting from velocities are  $\delta_{ge,v} = -2\pi \cdot 513$  MHz and  $\delta_{er,-v} = 2\pi \cdot 829$  MHz.

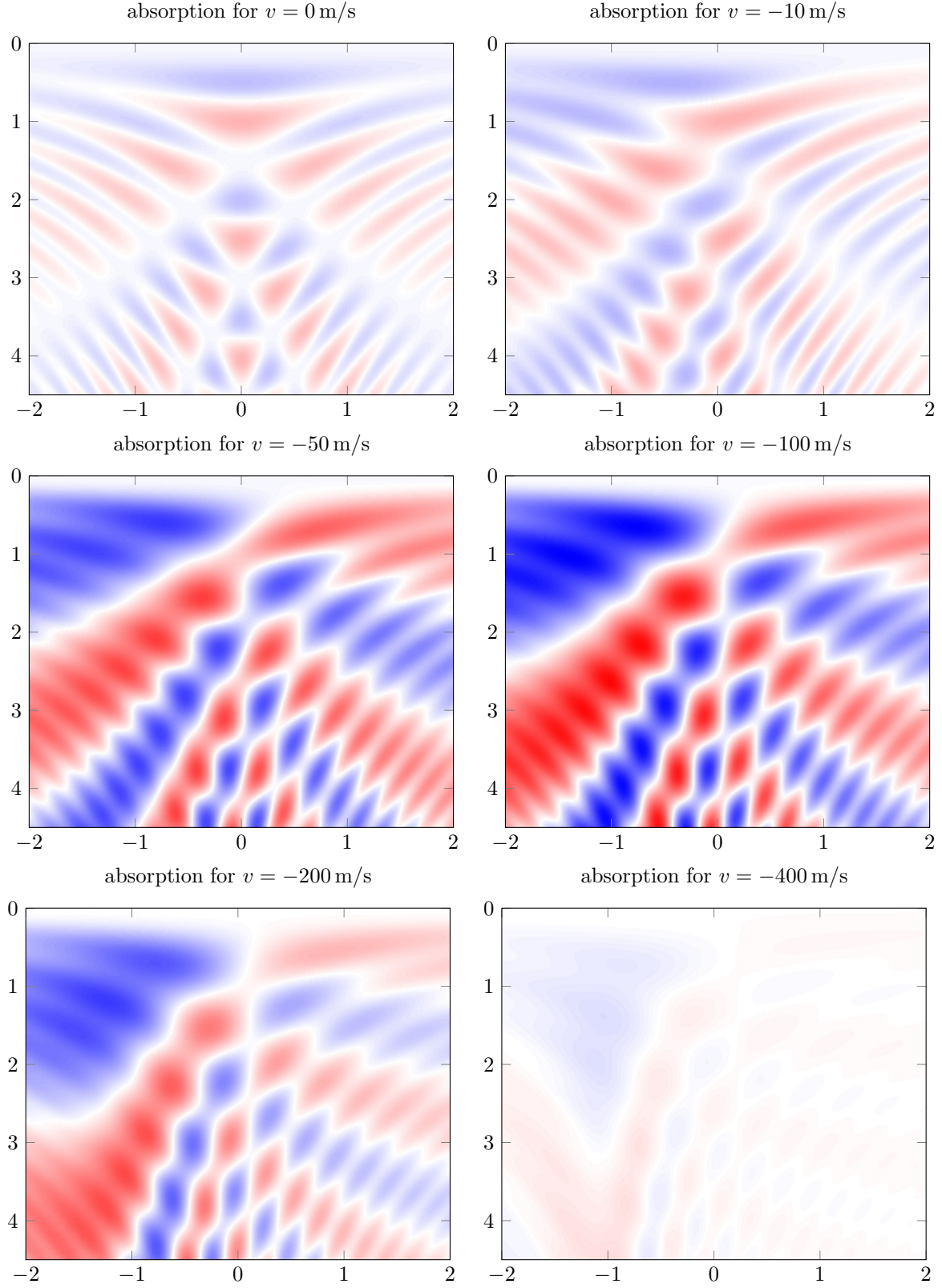


Figure 5.7.: Simulated absorption spectrum for different velocity classes weighted with the corresponding Maxwell-Boltzmann distribution factor for  $T = 120$  °C.  
x-axis:  $\delta_{er}$  [ $2\pi$  GHz], y-axis: time [ns], color code:  $\text{Im } \rho_{eg}$  in a.u.

### 5.2.2. Pulse shape dependence

Up to now we used a rectangular pulse shape for instructional purpose. With the given experimental setup only a Gaussian-like pulse shape is accessible. The transition from a rectangular pulse shape to the real one will explain the difference of the previous simulations to the experimental data. Mainly two aspects have to be taken into account:

- as the pulse intensity is varying temporally, the Rabi frequency changes accordingly
- the Autler-Townes splitting depends on the pulse intensity  $\Delta E = \hbar \sqrt{\Omega_{er}^2 + \delta_{er}^2}$  (see equation 2.32) and thus the splitting changes during the interaction

In order to visualize these effects, the peak Rabi frequency of the Gaussian-like pulse ( $\Omega_{er} = 2\pi \cdot 2 \text{ GHz}$ ) is divided into six equally spaced intensities as shown in figure 5.8. For low Rabi frequencies ( $\Omega_{ge} < 2\pi \cdot 1 \text{ GHz}$ ) the resonances of the Autler-Townes doublet are probed within the scan range. The oscillations are slow due to the low Rabi frequency and the low detunings from the Autler-Townes levels. With an increased Rabi frequency the oscillations frequency increases due to the Rabi frequency itself and due to the increased splitting causing a higher detuning.

One has to be aware that the final dynamics for a Gaussian pulse is not a sum over all shown intensities. Instead the dynamic starts at a low intensity, rises up to the peak intensity and returns to a low one again, according to the pulse shape.

The difference between a rectangular and a Gaussian pulse shape together with two intermediate states is shown in figure 5.9. Note that the pulse is not shown in its full length but the first 4.5 ns are displayed as for the experimental data. The pulse intensities for the non-Gaussian pulses are chosen such that at  $t = 4.5 \text{ ns}$  the same oscillatory phase is achieved as for the Gaussian pulse in order to be comparable to each other. Due to the averaging effect of the different intensities during the pulse only the slow mode remains, the faster one vanishes. The final simulation reproduces the experimental data (compare figure 4.4).



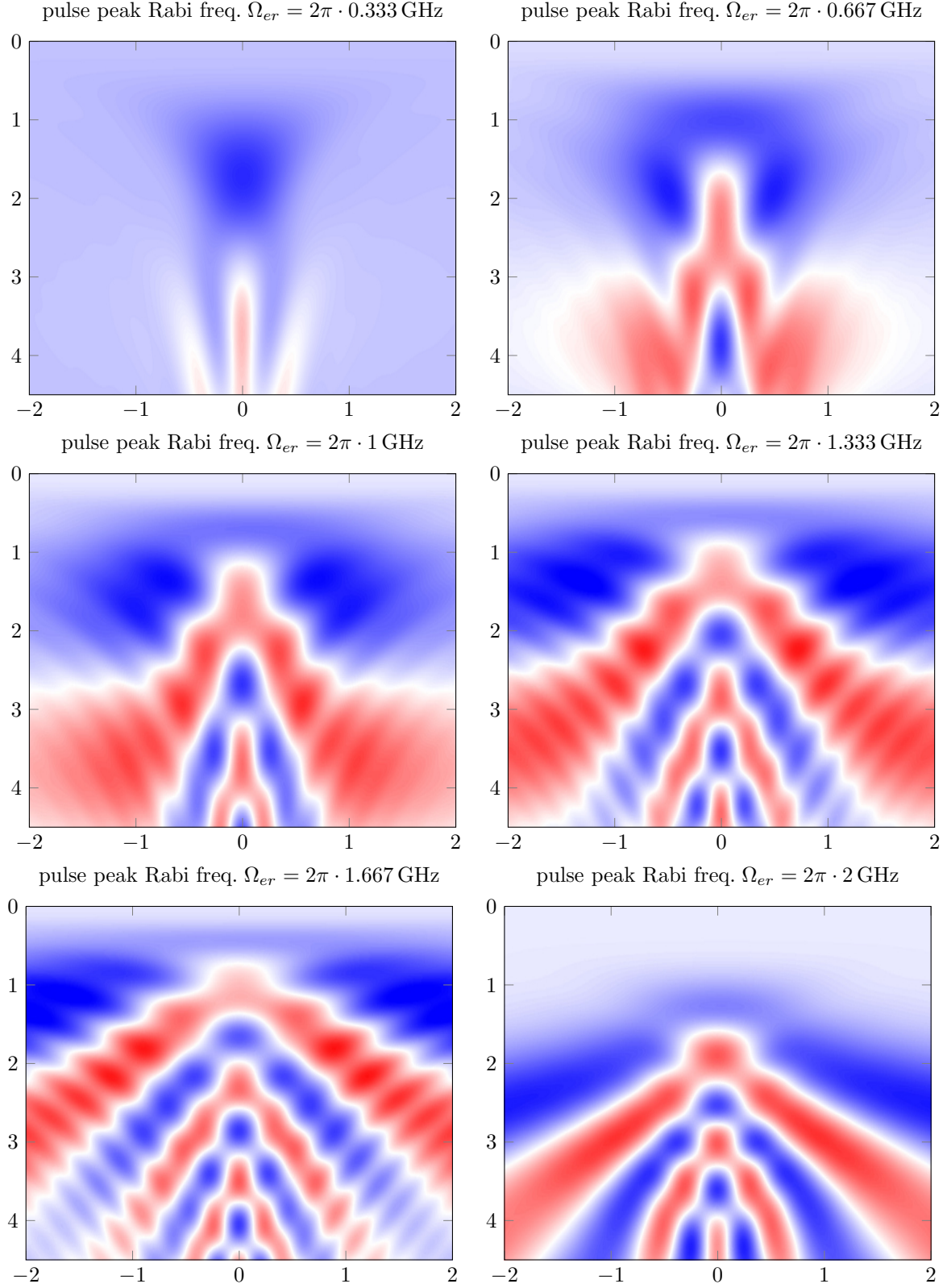


Figure 5.8.: Simulated absorption spectrum for a rectangular pulse shape at different pulse Rabi frequencies  $\Omega_{er}$ .

x-axis:  $\delta_{er}$  [2π GHz], y-axis: time [ns], color code:  $\text{Im } \rho_{eg}$  range:  $\pm 0.17$

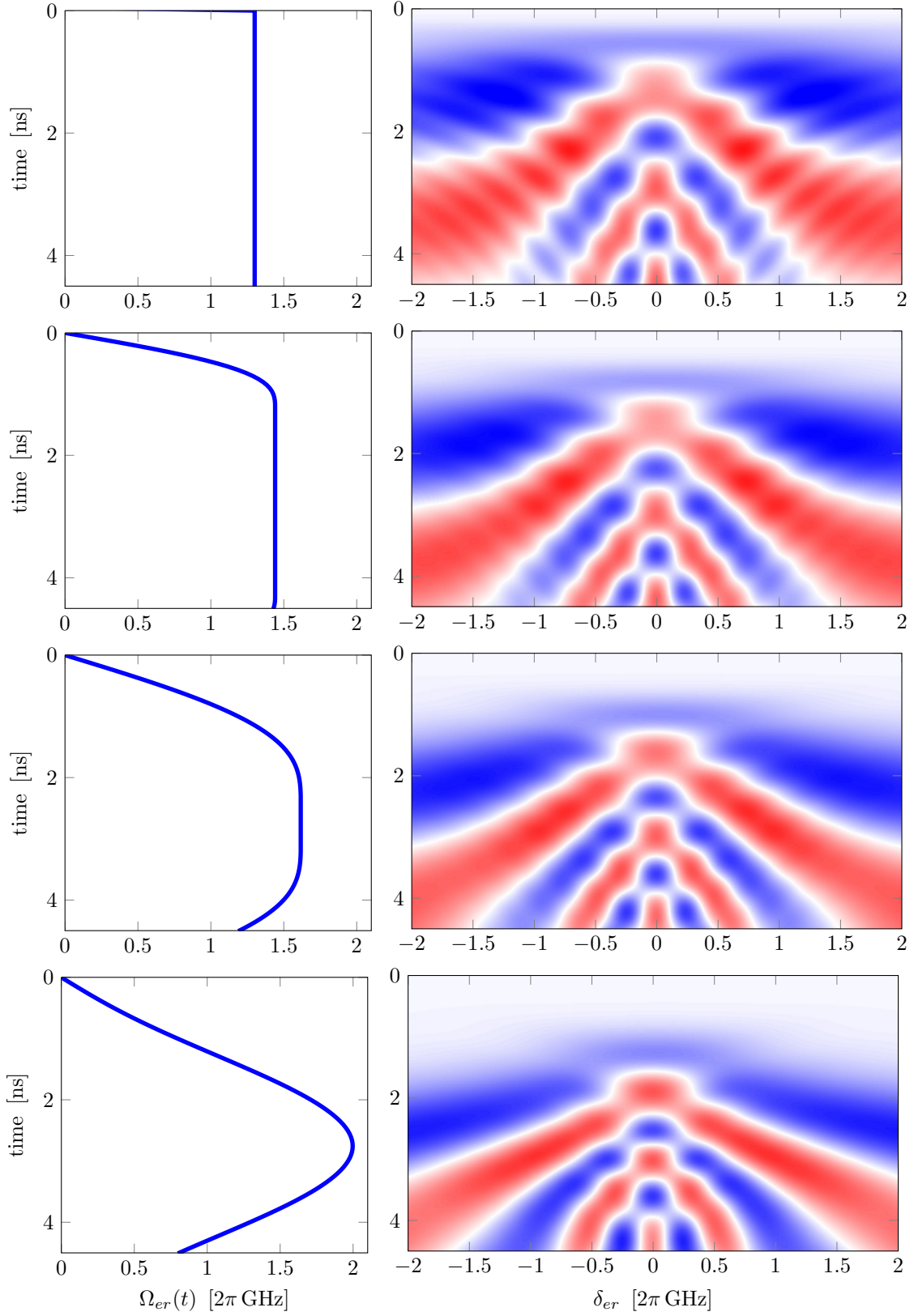


Figure 5.9.: Simulated absorption spectrum for different pulse shapes.  
color code for plots on the right:  $\text{Im } \rho_{eg}$  range:  $\pm 0.17$



### 5.2.3. Angular dependence

The visibility of the oscillations depends on the crossing angle between both lasers as illustrated in figure 5.10. In a co- or counter-propagating setup the absolute value of the velocity is the same for each atom in respect to the lasers. A co-propagating setup has a weak visibility since a Doppler shift causes a detuning of each transition in the same direction and thus increases the total detuning. For a perpendicular setup both detunings are independent of each other and hence the signal washes out. In contrast, a counter-propagating setup has the best visibility since both detunings are connected to each other as for the co-propagating setup, but instead of increasing the detuning it is partly compensated by the opposite laser. With an angle of  $171.5^\circ$  as used in the experiment (see section 3.4) a high visibility is obtained.

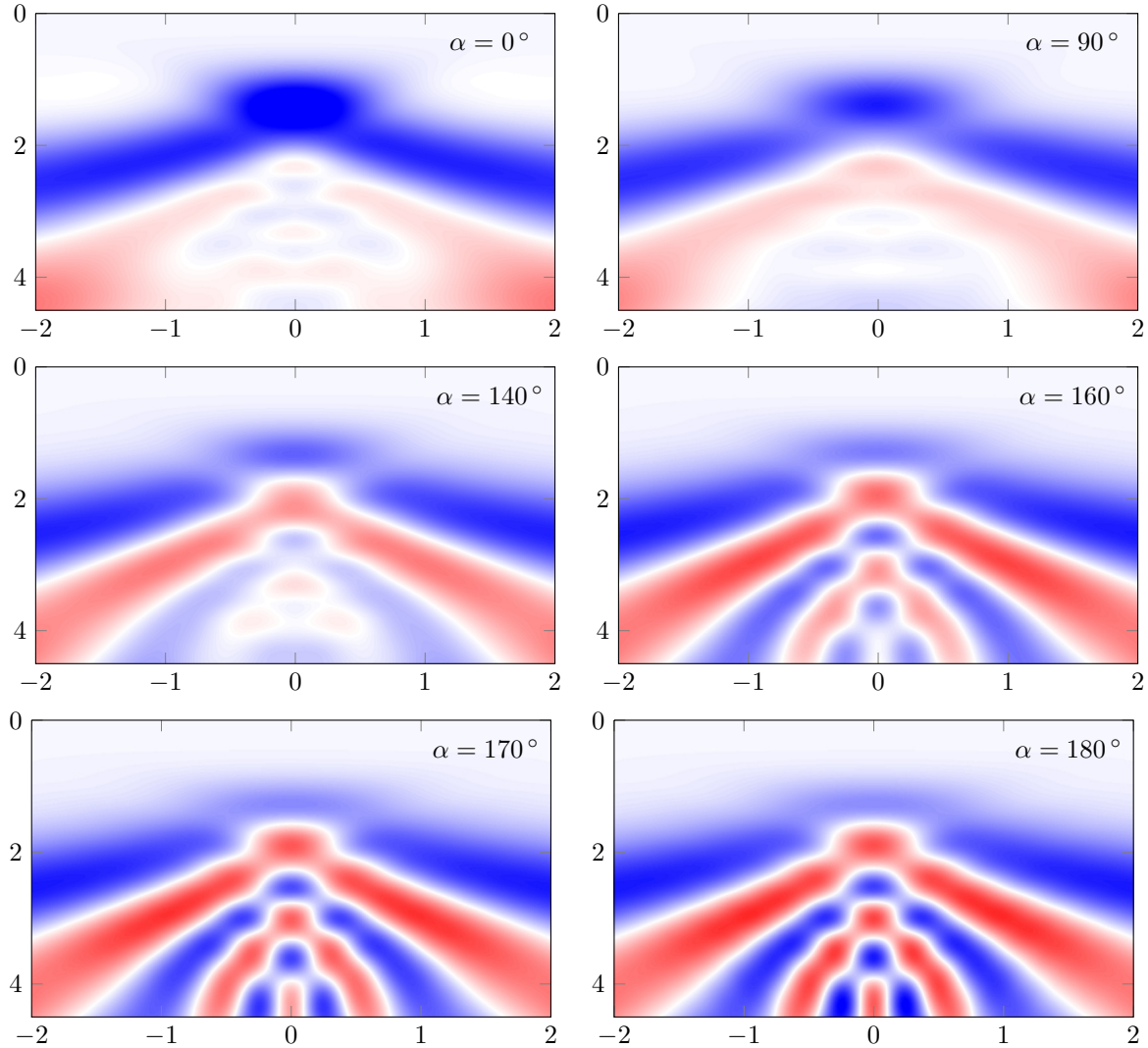


Figure 5.10.: Simulated absorption spectrum for different crossing angles of the beams.  
 x-axis:  $\delta_{er}$  [ $2\pi$  GHz], y-axis: time [ns], color code:  $\text{Im } \rho_{eg}$  range:  $\pm 0.17$

### 5.2.4. Temperature dependence

In order to change the atomic density inside the sample the temperature of the rubidium cell can be changed as presented in section 3.4. But a change in temperature also has an impact on the Doppler velocity distribution and hence on the absorption signal as simulated in figure 5.11. The standard deviation for the Doppler distribution is given in equation (5.13)  $\sigma_v \propto \sqrt{T}$ . At room temperature the relative temperature change on the Kelvin scale is small and causes only a small change in the Doppler profile. Hence almost no effects of heating or cooling the system can be seen at this temperature. Note that at  $T = 0$  K the only remaining velocity class is  $v = 0$  and hence no averaging effect due to the Doppler distribution takes place.

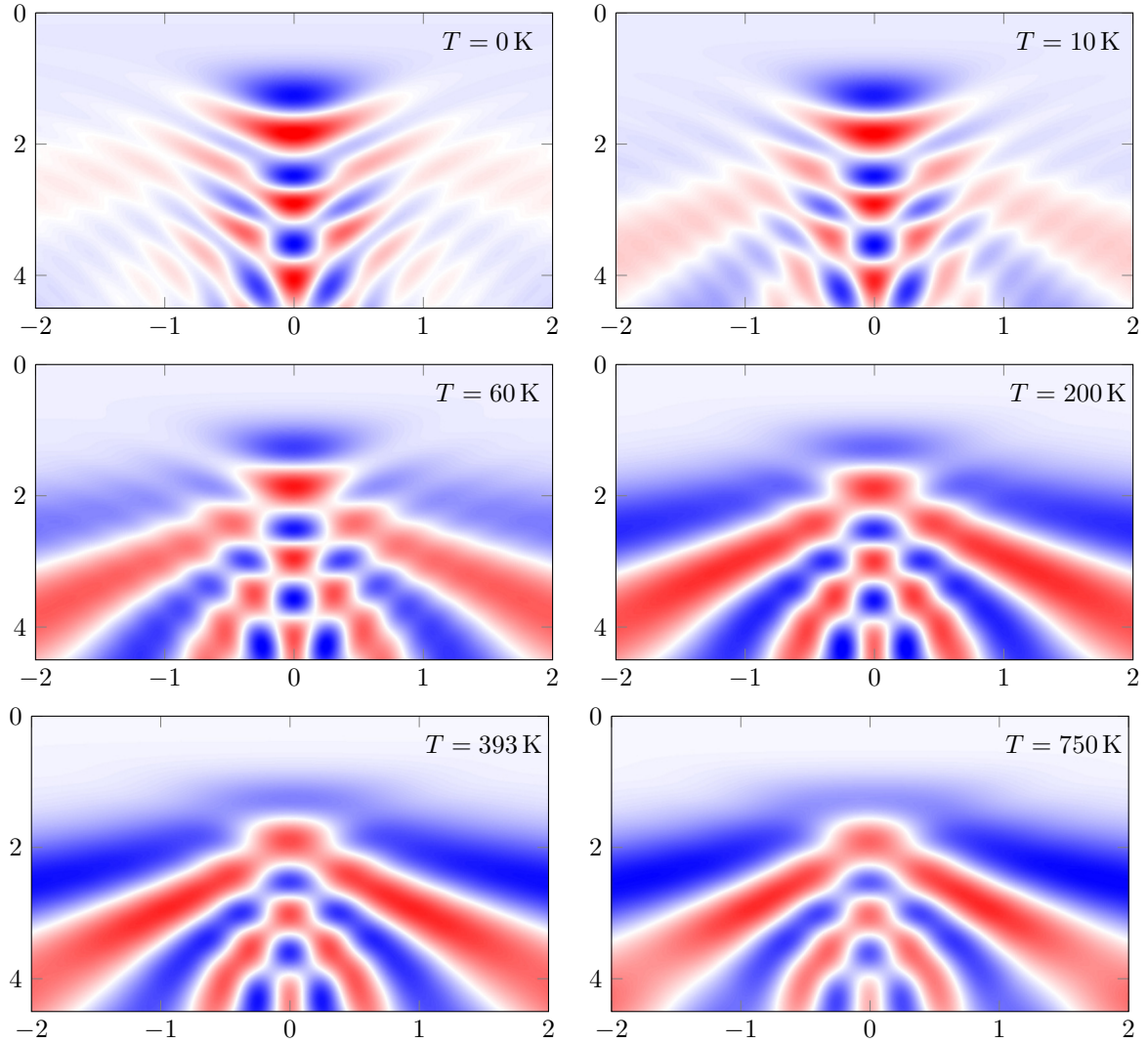


Figure 5.11.: Simulated absorption spectrum for different temperatures.

x-axis:  $\delta_{er}$  [ $2\pi$  GHz], y-axis: time [ns], color code:  $\text{Im } \rho_{eg}$  range:  $\pm 0.16$

### 5.3. Further development

The long-term goal of the work presented is to build quantum devices using the principle of fast coherent dynamics shown in this thesis even at room temperature. In order to realize single photon sources [34] and quantum gates [11], the setup of this experiment has to be adapted in a way that the Rydberg-Rydberg interaction emerges so that the Rydberg blockade effect [35] dominates.

Up to now an effective atomic density of  $\sim 1.3 \cdot 10^{12} \text{ cm}^{-3}$  is used in the experiment (see section 4.1). The density of atoms which can be excited to the Rydberg state is less due to the maximum Rydberg population reached (35 %) in this excitation scheme. So roughly a Rydberg density of  $5 \cdot 10^{11} \text{ cm}^{-3}$  is reached in the presented experiment.

In order to see the Rydberg blockade, the addressable atoms must have at most a distance less than the blockade radius here coarsely defined by the frequency shift due to the Rydberg-Rydberg interaction in range of the bandwidth of the experiment ( $\sim 2 \text{ GHz}$ , see section 5).

The frequency shift of rubidium-rubidium molecules is extracted from calculations for these molecules of the 35S, 45S and 55S states [36] and extrapolated as presented in figure 5.12. To determine the average distance to the next neighbor a simulation was performed for a non-interaction ideal gas where the atoms were randomly placed in a volume according to the density given (see figure 5.13). In a simple cubic lattice one would have a distance to the next neighbor of  $d = \sqrt[3]{1/\rho}$ , where  $\rho$  is the atomic density. With respect to the simulation the average next neighbor distance is 40 % less than in a cubic lattice.

In the experiment, the average distance of two neighboring Rydberg atoms is according to the effective density about  $0.75 \mu\text{m}$ . The blockade radius for a level shift of  $2 \text{ GHz}$  for the 30S state is about  $0.5 \mu\text{m}$ , which is already close to the average distance to the next neighboring atom.

In order to enter the blockaded regime one possibility is to increase the principal quantum number  $n$ . A state above 45S has a blockade radius greater than  $1 \mu\text{m}$  which should be sufficient to see the blockade. One has to find a rubidium Rydberg state in which the corresponding molecular state of the Rydberg atoms is well separated from any other state in order to see the blockade. Another possibility to reach higher interaction is to increase the temperature and hence the atomic density leading to a smaller distance between the atoms. To cut the distance between two atoms to half an increased density by a factor of  $2^3$  is required. This can be achieved by heating the sample by  $40 \text{ K}$ . Here the molecular states also have to fit so that the blockade can be seen. The indicator to be in the blockaded

regime is an asymmetrical absorption profile in respect to the detuning  $\delta_{er}$  and an increased Rabi frequency  $\Omega'_{er}$  due to a collective enhancement [37].

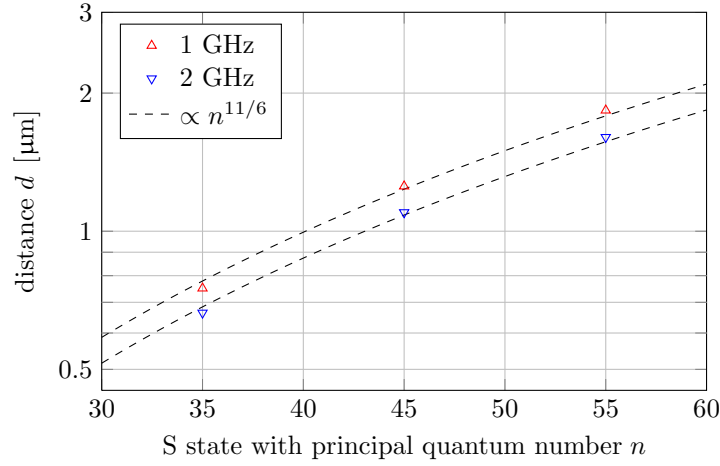


Figure 5.12.: Distance between two rubidium atoms for a level shift of the Rydberg state of 1 GHz (red) and 2 GHz (blue) [36]. The dashed lines show the proportionality  $n^{11/6}$  according to theory.

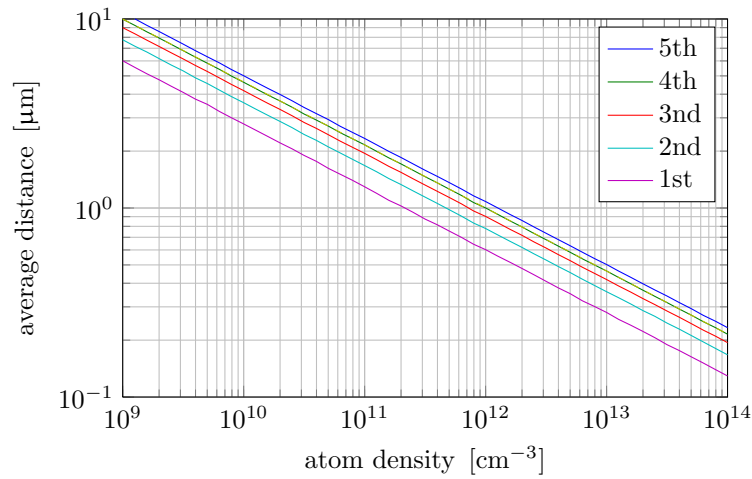


Figure 5.13.: Average distance to the  $n$ -th neighbor simulated for an ideal gas. The simple cubic lattice has the same next neighbor distance as the averaged forth neighbor of a random sample.

## 6. Summary and Outlook

The results presented in this thesis give certainty that fully coherent dynamic processes involving Rydberg states can be realized in a cell of rubidium vapor even above room temperature. In the experiment a bandwidth-limited pulsed excitation with a pulse duration of  $\sim 4$  ns was used to couple to the Rydberg state. During the pulse, six full Rabi cycles to the Rydberg state could be observed resulting in a peak Rabi frequency of  $\sim 2.3$  GHz. Due to this high Rabi frequency the thermal gas inside the cell can be regarded as frozen on the relevant timescale.

Despite the complicated level structure of rubidium it has been shown that a simple three-level system is capable of describing the dynamics observed in the experiment: due to the bandwidth of the experiment ( $\sim 2$  GHz) and the transitions chosen the level scheme of rubidium can be reduced to the transition from the ground state  $5S_{1/2} F = 2$  to the excited state  $5P_{3/2}$  and from there to the Rydberg state  $30S_{1/2}$ . The hyperfine levels of the excited state are close together ( $\sim 100$  MHz) and thus are treated as one as they are not resolved. For the experiment the lower transition is driven by a cw probe laser (780 nm) of which the transmission is measured. The upper transition is driven by a pulsed laser (480 nm) to reach the high intensities required to compensate for the weak dipole matrix element of this Rydberg transition. High Rabi frequencies on the gigahertz range are required due to the coherence time of up to a couple of nanoseconds.

At first the dependency of Rabi oscillations on the intensity  $I_{er}$  of the upper transition was studied. A square root like behavior  $\Omega_{\text{eff}} \propto \sqrt{\Omega_{ge}^2 + a I_{er}}$  was observed as expected for a three-level system with both transitions resonantly driven. Furthermore the system was examined for different detunings  $\delta_{er}$  of the upper transition. The experimental data showed the fastest oscillations for both transitions on resonance. With an increasing detuning  $|\delta_{er}|$  the oscillations became slower which is different from a two-level system where the Rabi frequency increases with the detuning  $\Omega_{\text{eff}} = \sqrt{\Omega_{er}^2 + \delta_{er}^2}$ .

In order to get an insight into the physical mechanisms the three-level atom was simulated even in a more simplified system: the pulse shape was assumed to be rectangular. With

that the dominating effect describing the dynamic of the experiment, an Autler-Townes splitting together with the influence of the Doppler shift of the atoms, could be studied in detail. It turns out that atoms with a velocity of  $|v| \simeq 100$  m/s have the highest impact on the absorption signal. Significantly faster atoms are rare due to the Doppler distribution and atoms at rest or of low velocities are high in numbers but out of resonance due to the anticrossing of the Autler-Townes splitting.

Furthermore the influence of the pulse shape was examined. For a rectangular pulse the Autler-Townes splitting is constant whereas for a Gaussian-like pulse as used in the experiment the splitting changes during the interaction time. Thus the faster oscillatory mode out of the two from the Autler-Townes doubled washes out and only the slow one remains. Additionally the dependence of the crossing angle of the two laser beams was examined. The best signal can be observed in counter-propagating direction since the velocities of the atoms have the lowest impact here. Within a deviation angle of  $\pm 15^\circ$  the visibility almost does not change. For experimental reasons one laser was slightly rotated by  $8.5^\circ$  to avoid an overlap at the cell surface with the second laser.

Another parameter of the system is the temperature. Heating or cooling has an influence on the Doppler distribution and hence on the absorption signal. For the experiment at a temperature of  $T \simeq 120^\circ\text{C}$  a change of  $\pm 100$  K has almost no influence on the absorption signal which is due to the small relative change of the Doppler distribution  $\sigma_v \propto \sqrt{T}$ .

As a last result the Rydberg blockade radius of the current experiment was estimated and the average distance between two neighboring atoms simulated. It turns out that the distance between atoms in the Rydberg state is already close to the Rydberg blockade radius. In order to estimate the change required to enter the blockaded regime the dependency of the atomic density and the distance of two neighboring atoms was studied. Moreover the level shift for different principal quantum number  $n$  was examined. The rubidium molecular states show a non-trivial behavior in the blockade distance. Some of the states mix depending on the Rydberg state which can suppress the blockade. Further studies will be required.

The final step after the blockaded regime will be reached is to decrease the cell volume to a size where only one excitation can exist in one cell [8]. Here the interaction of the atoms and the wall of the cell is an issue. It has been shown that certain principal quantum numbers  $n$  cause only weak wall-induced effects and hence are candidates for a use in these cells [38]. Finding an appropriate Rydberg state is crucial to satisfy all constraints for the wall interaction and the Rydberg blockade radius including the molecular states.

This thesis provides measurements that suggest a thermal gas of rubidium as a system for the physical realization of a quantum system. The basic requirements, the coherent dynamics, could be observed in the experiment. This builds the basis for a further development of different quantum devices in a thermal gas of rubidium as quantum gates [11], single photon emitters [34] or absorbers [39].

The next steps for a further development of this new approach are sketched and with certainty there will be a lot of interesting physics to investigate in order to finally realize a scalable quantum device.

# A. Level scheme and $D_1/D_2$ absorption spectrum of Rubidium

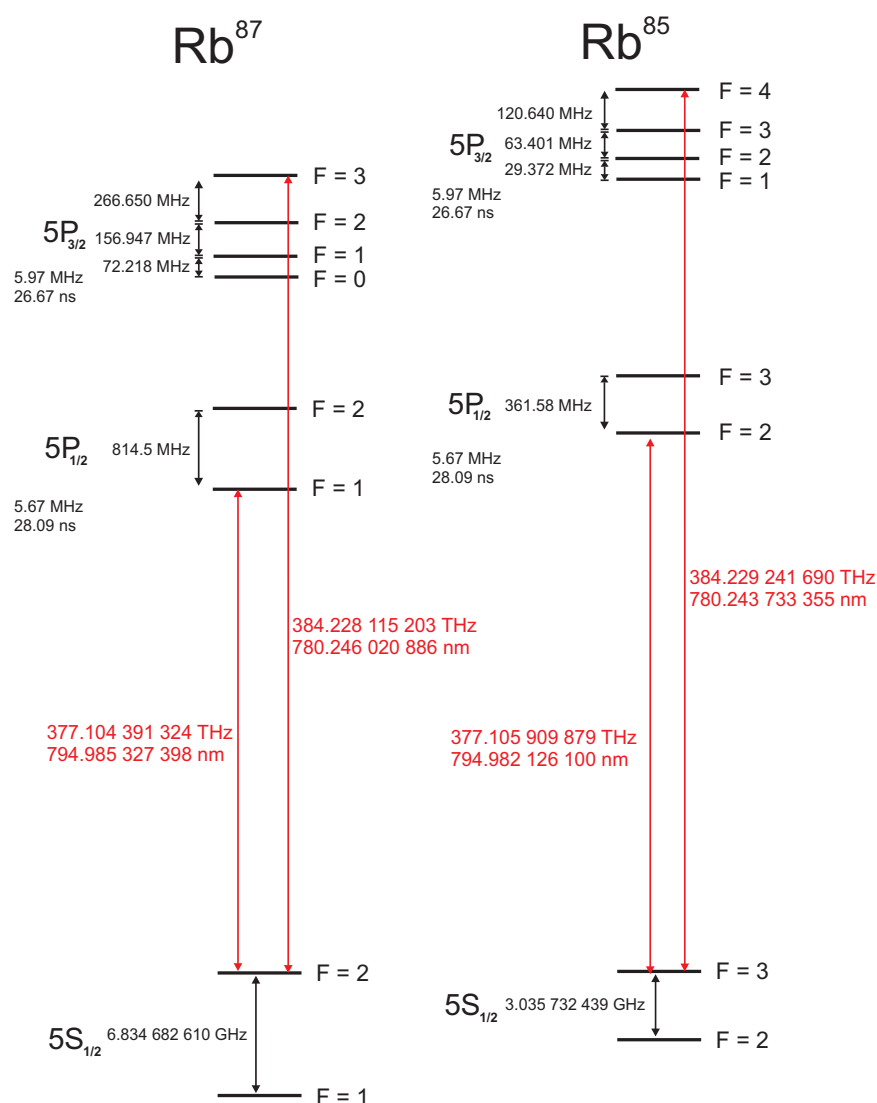


Figure A.1.: Ground state transitions of rubidium  $^{87}\text{Rb}$  and  $^{85}\text{Rb}$  [40].



A. Level scheme and  $D_1/D_2$  absorption spectrum of Rubidium

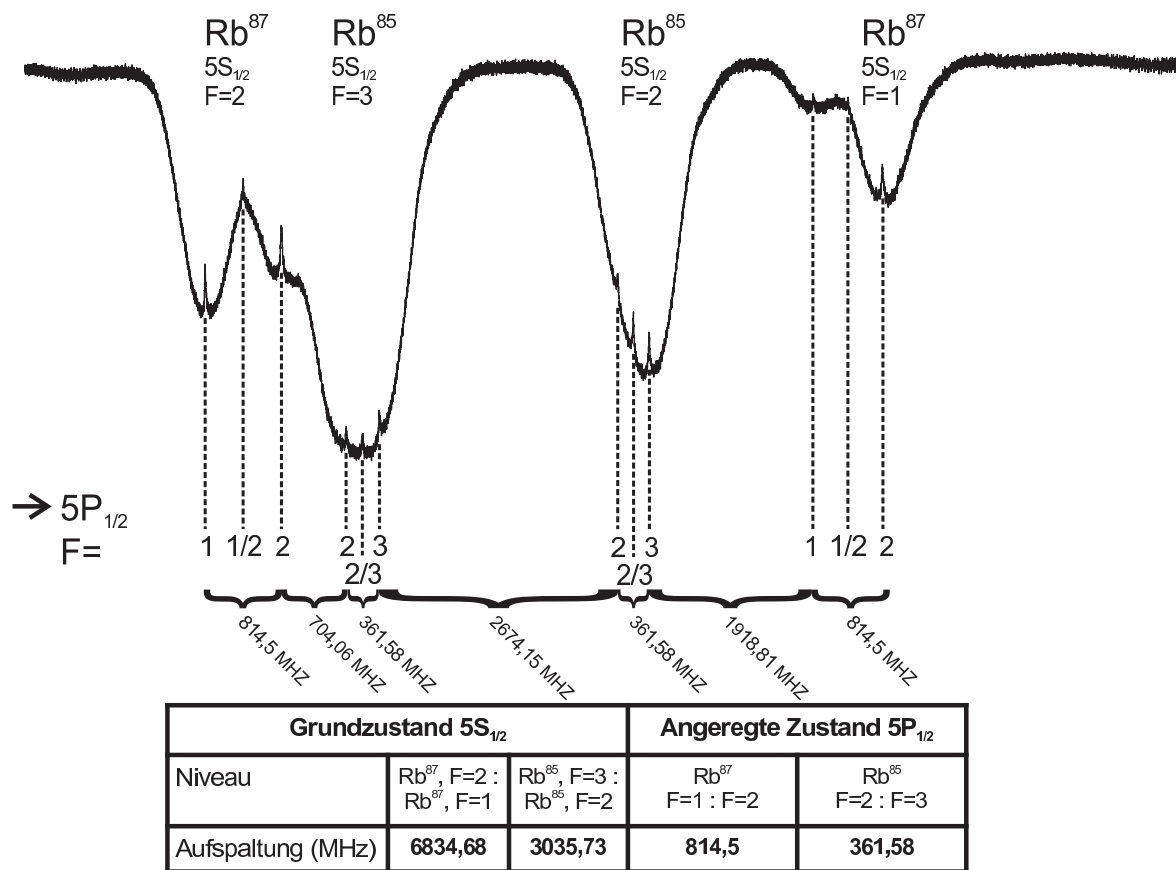


Figure A.2.: Absorption spectrum of  $D_1$  line ( $5S_{1/2} \rightarrow 5P_{1/2}$ )

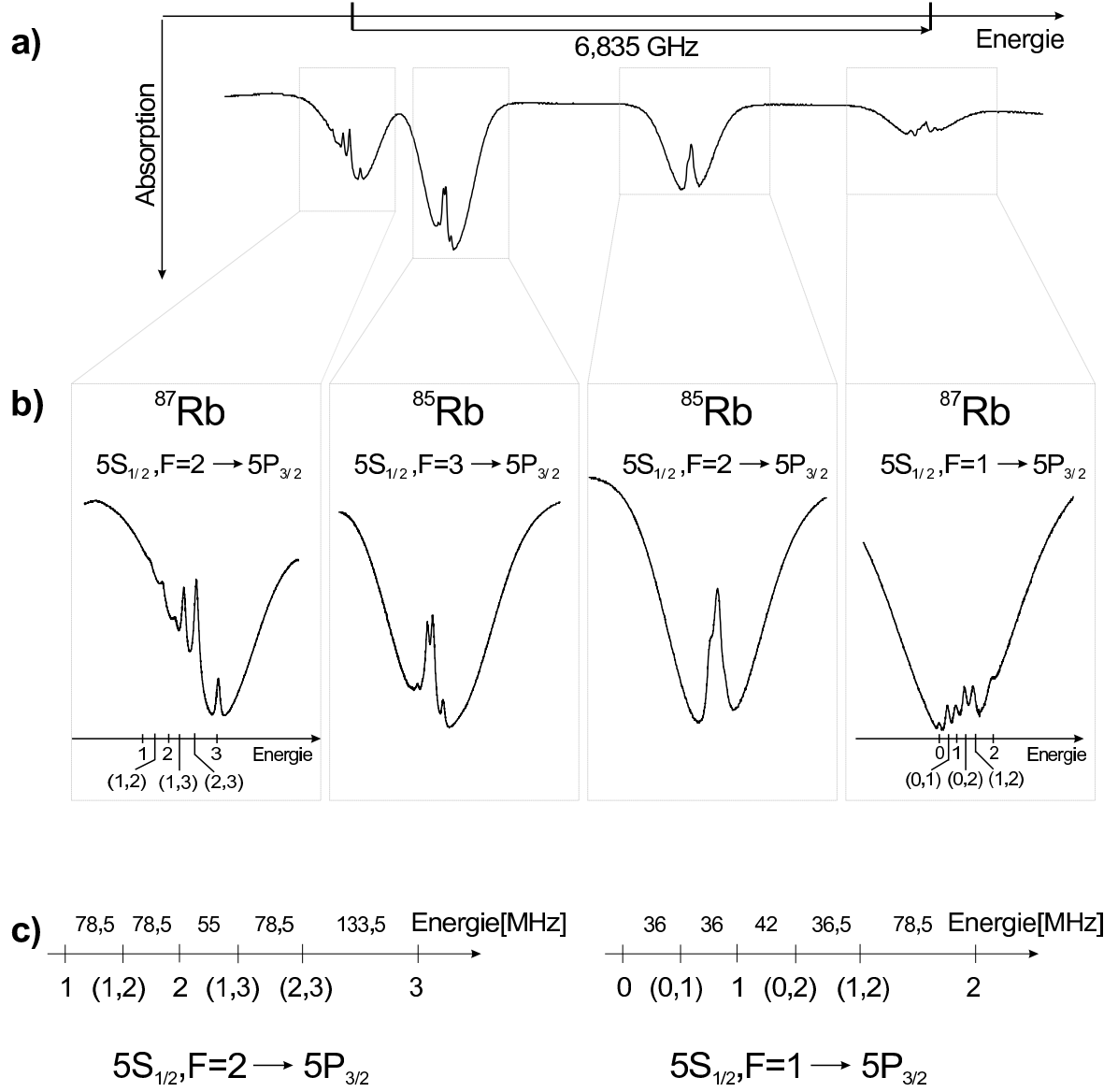


Figure A.3.: Absorption spectrum of  $D_2$  line ( $5S_{1/2} \rightarrow 5P_{3/2}$ ) [41]

## B. Simulation details

### B.1. Solving differential equations numerically

The ordinary differential equation which describes the time development of the density matrix as introduced in chapter 5

$$\frac{\partial \rho}{\partial t} = -\frac{i}{\hbar}[H, \rho] \quad (\text{B.1})$$

is well suited to be solved by numerical integration. Two approaches will be presented: a simple one (Euler method) and a powerful widespread approach (Runge-Kutta method).

The simplest numerical integration algorithm is the Euler method. Let us assume we have a differential equation

$$\frac{\partial y(t)}{\partial t} = y(t), \quad (\text{B.2})$$

which is integrated analytically to  $y(t) = e^t$  with the initial condition  $y(0) = 1$ . For finite time steps this differential equation can be transformed to a difference equation

$$\frac{\Delta y}{\Delta t} = y \quad \rightarrow \quad \Delta y = y \Delta t. \quad (\text{B.3})$$

The differential equation is approximated by

$$y[t+1] := y[t] + \Delta y[t, y[t]]. \quad (\text{B.4})$$

For a time step of  $\Delta t = 1$  and the given initial condition the discrete calculated values are

$t$	$y[t]$	$\Delta y[t]$	$y[t+1]$
0	1	1	2
1	2	2	4
2	4	4	8

The comparison between the discrete and analytical integration is shown in figure B.1. The chosen time step  $\Delta t = 1$  leads to a coarse approximation of the given differential equation. The accuracy would increase by using smaller time steps.

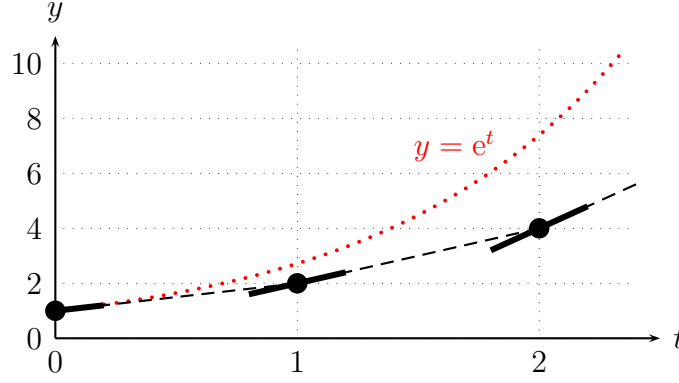


Figure B.1.: Numerical integration of  $y' = y$  using the Euler method.

The idea of the Euler method is improved by the Runge-Kutta algorithm (here presented in forth order), which is used in *Mathematica* as default algorithm to solve differential equations numerically. The calculation rule and the calculated values for the example  $y' = y$ ,  $\Delta t = 2$  are

$$\frac{\partial y}{\partial t} = f(t, y) \quad (\text{B.5})$$

$$y[t + 1] := y[t] + \frac{1}{6}(a_1 + 2a_2 + 2a_3 + a_4)\Delta t \quad (\text{B.6})$$

$$a_1 = f(t, y) \quad (\text{B.7})$$

$$a_2 = f\left(t + \frac{\Delta t}{2}, y + \frac{\Delta t}{2}a_1\right) = f\left(t + \frac{\Delta t}{2}, y_1\right) \quad (\text{B.8})$$

$$a_3 = f\left(t + \frac{\Delta t}{2}, y + \frac{\Delta t}{2}a_2\right) = f\left(t + \frac{\Delta t}{2}, y_2\right) \quad (\text{B.9})$$

$$a_4 = f(t + \Delta t, y + \Delta t a_3) = f(t + \Delta t, y_3) \quad (\text{B.10})$$

coeff.	$a_n$	$y_n$	$a_n$
	$a_1$	1	1
	$a_2$	2	2
	$a_3$	3	2.5
	$a_4$	7	7

With these coefficients the new value of  $y$  can be calculated:

$$y[t = 2] = 1 + \frac{1}{6}(1 + 2 \cdot 2 + 2 \cdot 2.5 + 7) \cdot 2 = 5 \quad (\text{B.11})$$

The Runge-Kutta method will be explained with the graphical scheme of figure B.2. The first part of the algorithm is similar to the Euler method. First the coefficient  $a_1$  is calculated (equation B.7) with a value according to the given differential equation  $y' = y$ ,  $y = 1 \rightarrow a_1 = 1$ . With this new slope half a time step is executed illustrated by the dashed line. At the new position the differential equation is evaluated (B.8) and gives  $a_2 = 2$ . This is the new slope (indicated by the arrow) for another half step starting again from  $t = 0$ . This third position is evaluated again (B.9) giving the slope  $a_3 = 3$  for the last (full) step performed which starts again at  $t = 0$ . Here the fourth coefficient  $a_4$  (B.10) can be calculated. Now a weighted average (B.6) gives the slope for the integration and the final position is reached, highlighted as the thick dot in the diagram. This algorithm results in a higher accuracy compared to the Euler method. The Runge-Kutta method outperforms the Euler method due to a smaller error: the error per step for the Euler method is of order  $(\Delta t)^2$  whereas for the Runge-Kutta method it is  $(\Delta t)^5$ .

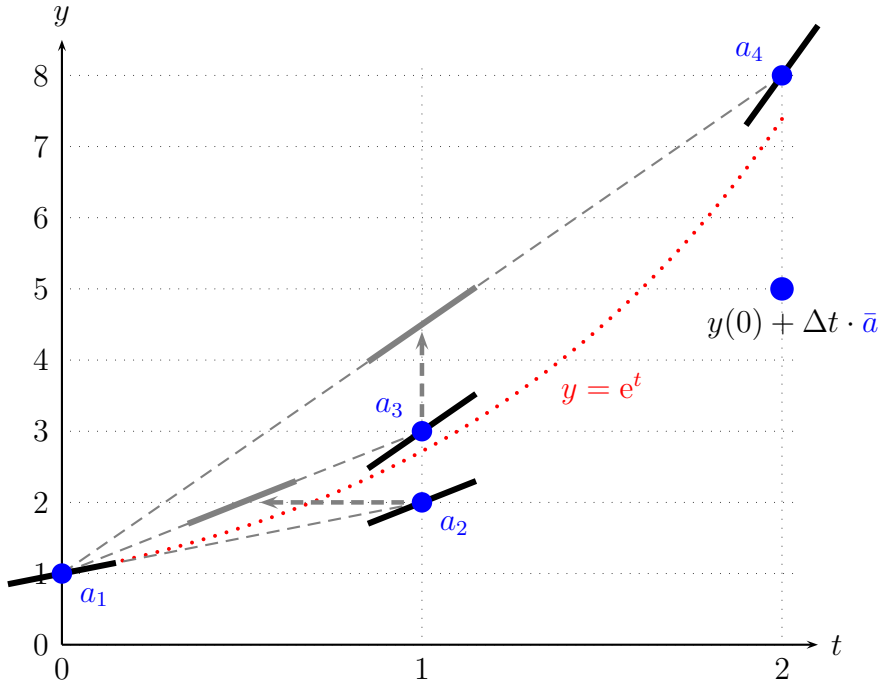


Figure B.2.: Numerical integration of  $y' = y$  using the Runge-Kutta method.

## B.2. Simulation in Java

In this section the core source code for the simulation of the density matrix in time is shown. This is possible since the differential equation for a three-level atom is only a system of nine first order differential equations. These equations can be further reduced since the density matrix is Hermitian. As a drawback, *Java* cannot handle complex numbers. Hence the equations are solved for their real and imaginary part separately, which is denoted as `_Re` and `_Im` in the following. Note that the levels of the atoms are addressed by numbers not by letters ( $1 \hat{=} g$ ,  $2 \hat{=} e$  and  $3 \hat{=} r$ ). The initial condition is given by equation (5.5) and calculated at the initialization of the density matrix entries:

```
double Omega1_Init = Omega1_Sampled[0];
double denominator = 4 * Delta1 * Delta1 + Gamma12 * Gamma12
                    + 2 * Omega1_Init * Omega1_Init;
double Rho11_Re = 1 - Omega1_Init * Omega1_Init / denominator;
double Rho22_Re = 1 - Rho11_Re;
double Rho12_Re = 2 * Omega1_Init * Delta1 / denominator;
double Rho12_Im =      Omega1_Init * Gamma12 / denominator;
double Rho33_Re = 0;
double Rho13_Re = 0;
double Rho13_Im = 0;
double Rho23_Re = 0;
double Rho23_Im = 0;
```

The dynamic of the real system is described by the differential equation (5.3). Here the equation is solved by the Euler method since the code for the Runge-Kutta method does not give any new insights and is almost the same as the Euler one but repeated four times. The algorithm is divided into two parts. At first the slope is calculated (denoted as `D_`) for the next time step as presented in equation (B.4):

```
Omega1 = Omega1_Sampled[t];
Omega2 = Omega2_Sampled[t];

D_Rho11_Re = -(Rho12_Im * Omega1) + Gamma12 * Rho22_Re;
D_Rho22_Re =  Rho12_Im * Omega1 - Rho23_Im * Omega2
              - Gamma12 * Rho22_Re + Gamma23 * Rho33_Re;
D_Rho33_Re =  Rho23_Im * Omega2 - Gamma23 * Rho33_Re;

D_Rho12_Re = Delta1 * Rho12_Im - (Omega2 * Rho13_Im) / 2.
              - (Rho12_Re * Gamma12) / 2.;
D_Rho13_Re = (-2 * (0.5 * Omega2 * Rho12_Im - (Delta1 + Delta2) * Rho13_Im)
              + Rho23_Im * Omega1 - Rho13_Re * Gamma23) / 2.;
D_Rho23_Re = ( 2 * Rho23_Im * Delta2 + Rho13_Im * Omega1
              - Rho23_Re * (Gamma12 + Gamma23)) / 2.;

D_Rho12_Im = (-2 * Rho12_Re * Delta1 + Rho13_Re * Omega2
              - Rho12_Im * Gamma12 + Omega1 * (Rho11_Re - Rho22_Re)) / 2.;
```

## B. Simulation details

---

```

D_Rho13_Im = (0.5 * Omega2 * Rho12_Re - (Delta1 + Delta2) * Rho13_Re)
              - (Rho23_Re * Omega1) / 2. - (Rho13_Im * Gamma23) / 2.;
D_Rho23_Im = (-2 * Rho23_Re * Delta2 - Rho13_Re * Omega1
              - Rho23_Im * (Gamma12 + Gamma23) + Omega2 * (Rho22_Re - Rho33_Re)) / 2.;

```

In the second part of the algorithm the propagation takes place:

```

Rho11_Re += timeStep * D_Rho11_Re;
Rho22_Re += timeStep * D_Rho22_Re;
Rho33_Re += timeStep * D_Rho33_Re;

Rho12_Re += timeStep * D_Rho12_Re;
Rho13_Re += timeStep * D_Rho13_Re;
Rho23_Re += timeStep * D_Rho23_Re;

Rho12_Im += timeStep * D_Rho12_Im;
Rho13_Im += timeStep * D_Rho13_Im;
Rho23_Im += timeStep * D_Rho23_Im;

```

This is already the full source code to calculate the temporal evolution of the density matrix with *Java*. Since it is such a short code the performance of the Euler algorithm is outstanding and also of the Runge-Kutta method.

This model has also been extended to cover two or three interacting atoms. A performance comparison is given in the next section, the increase of lines of code is shown here:

atoms	density matrix	lines of code for Euler method
1	3x3	18
2	9x9	162
3	27x27	1458

### B.3. Performance of Mathematica, Java and C++

With *Mathematica* as a computational software program a vast variety of mathematical problems can be solved. But due to its universality its performance is slower than a native program solving specific equations. Here a performance comparison between *Mathematica* as a generic computational software, *Java* and *C++* which are native computer languages, is given. In order to compare the performance between the different tools a simulation for one, two and three atoms is performed using the Euler method to integrate the differential equation. The time step is chosen to be  $\Delta t = 10^{-10}$  s and the simulation duration is  $10^{-5}$  s. Therefore  $10^5$  time steps are calculated. The results are shown in the following table:

atoms	density matrix	calc. time [ms] <i>Mathematica</i>	calc. time [ms] <i>Java</i>	calc. time [ms] <i>C++</i>
1	3x3	$1 \cdot 10^4$	$3 \cdot 10^0$	$2 \cdot 10^0$
2	9x9	$2 \cdot 10^5$	$4 \cdot 10^1$	$2 \cdot 10^1$
3	27x27	n.a.	$1 \cdot 10^4$	$1 \cdot 10^2$

The simulations are computed on Intel Core i7 860 @ 2.80 GHz using a single core. Note that in the simulation for three atoms the implemented Hamiltonian has only one free parameter  $\delta_{er}$  and no decays are included. For the other simulations the decaying channels were implemented and the parameters  $(\Omega_{ge}, \delta_{ge}, \Gamma_{eg}, \Omega_{er}, \dots)$  could be changed.

The performance rates of the different solving methods are as expected. *Mathematica* at least  $10^3$  times slower than *Java* and *C++* as a generic solving tool. The only significant difference between *Java* and *C++* appears in the simulation for three atoms. Here the just-in-time compiler of *Java* cannot optimize the calculation significantly anymore and the precompiled *C++* simulation is much faster.



## **B.4. Various simulations**

On the following pages different simulations of basic experimental parameters are given:

- Detuning scan of cw laser  $\delta_{ge}$  (figure B.3)
- Rabi frequency scan of cw laser  $\Omega_{ge}$  (figure B.4)
- Detuning scan of pulse  $\delta_{er}$  (figure B.5)
- Rabi frequency scan of pulse  $\Omega_{er}$  (figure B.6)

The first two scans of the cw laser for the ground state transition are presented since they are not accessible in the experiment but can help to understand the whole system. The scan parameters of all four simulations were chosen to have higher intensities and frequencies than used in the experiment.

### Detuning scan of cw laser $\delta_{ge}$

$\delta_{ge}$ : see x-axis

$\Omega_{ge}$ :  $2\pi \cdot 0.2$  GHz

$\delta_{er}$ : 0 GHz

$\Omega_{er}$ :  $2\pi \cdot 2$  GHz

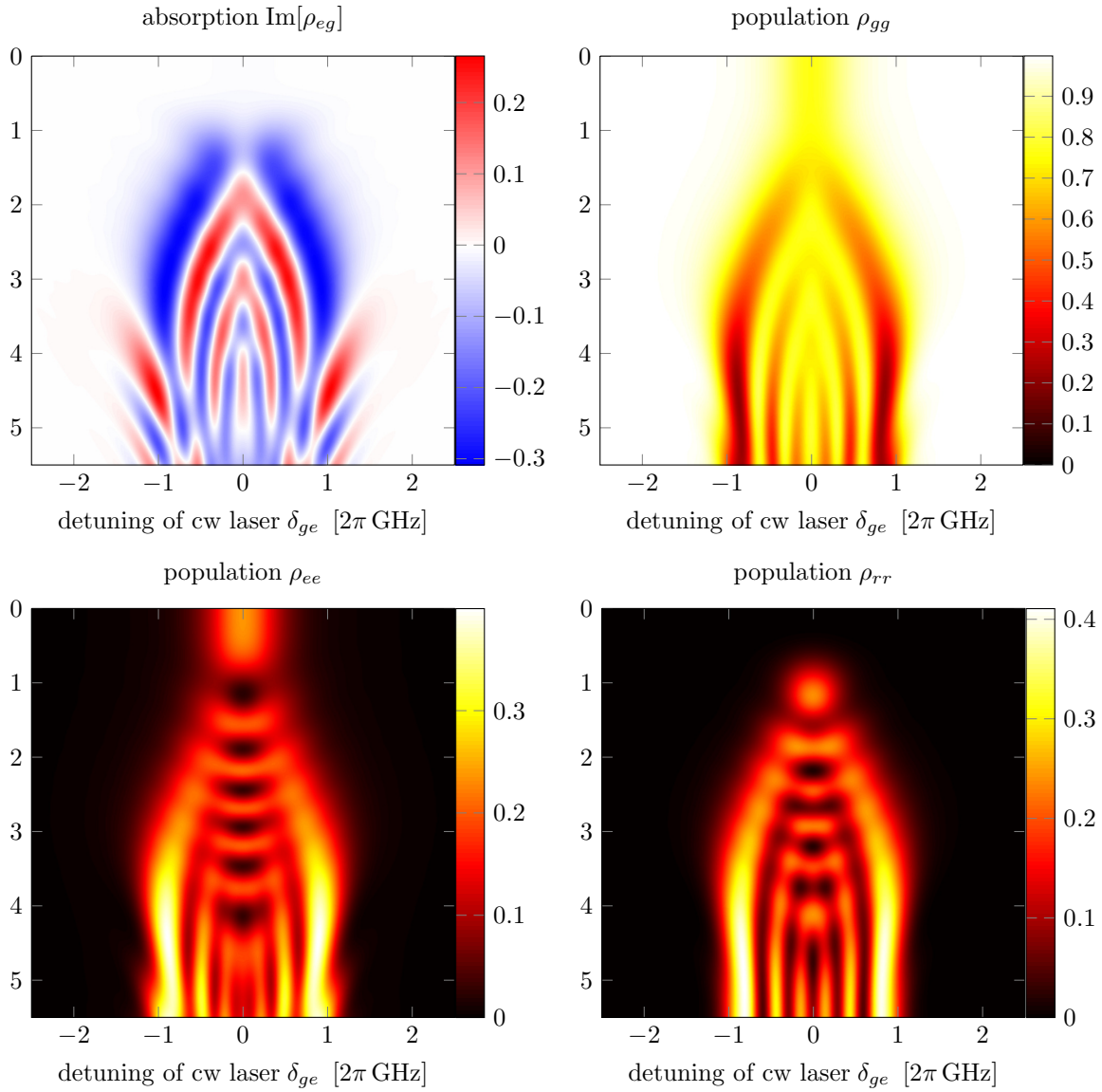


Figure B.3.: Detuning scan of pulse  $\delta_{ge}$ , y-axis: time [ns]

### Rabi frequency scan $\Omega_{ge}$ of cw transition

$\delta_{ge}$ : 0 GHz

$\Omega_{ge}$ : see x-axis

$\delta_{er}$ : 0 GHz

$\Omega_{er}$ :  $2\pi \cdot 2.2$  GHz

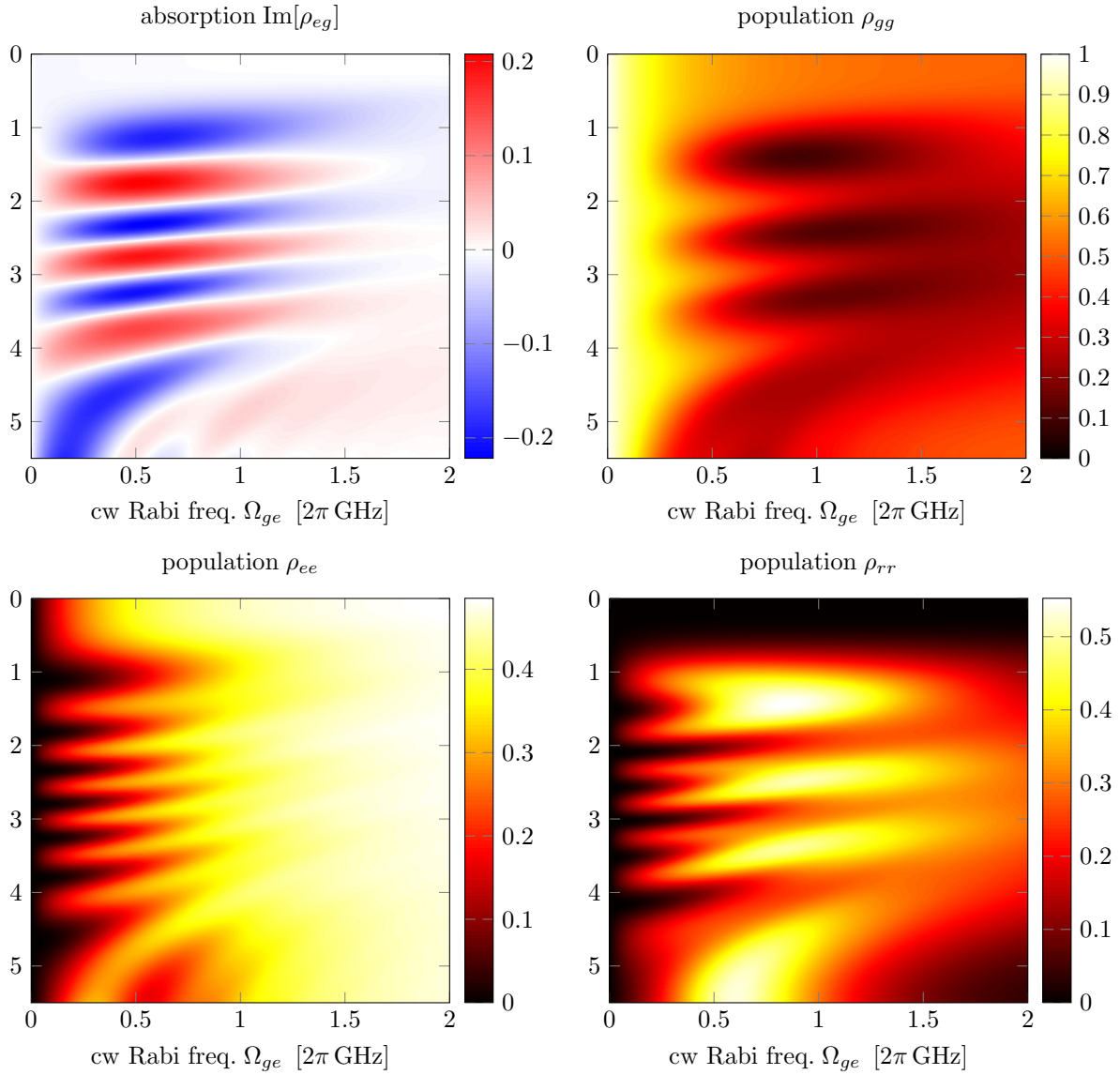


Figure B.4.: Rabi frequency scan  $\Omega_{ge}$  of cw transition, y-axis: time [ns]

### Detuning scan of pulse $\delta_{er}$

$\delta_{ge}$ : 0 GHz

$\Omega_{ge}$ :  $2\pi \cdot 0.2$  GHz

$\delta_{er}$ : see x-axis

$\Omega_{er}$ :  $2\pi \cdot 2$  GHz

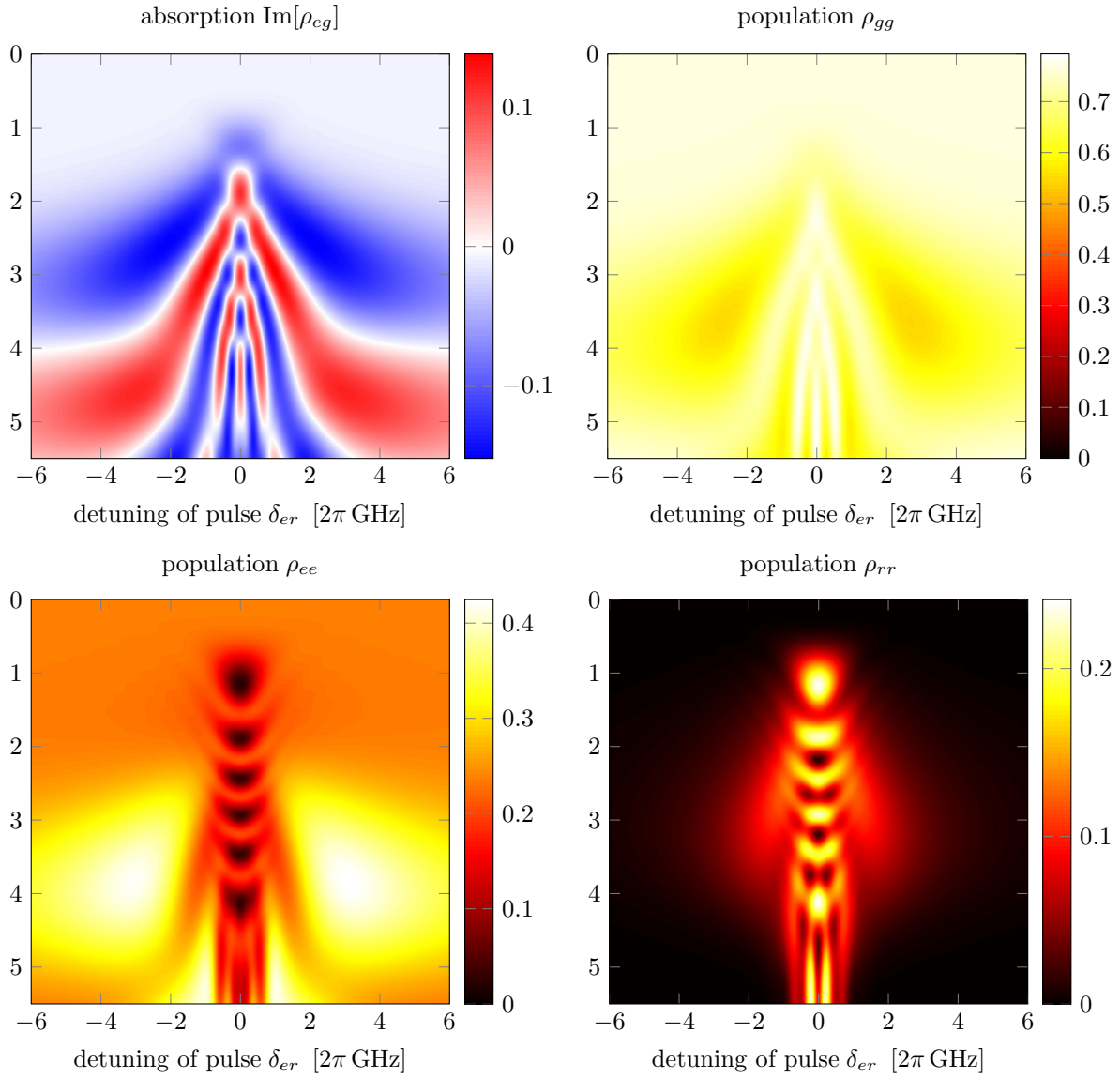


Figure B.5.: Detuning scan of pulse  $\delta_{er}$ , y-axis: time [ns]

**Rabi frequency scan of pulse  $\Omega_{er}$**

$\delta_{ge}$ : 0 GHz

$\Omega_{ge}$ :  $2\pi \cdot 0.2$  GHz

$\delta_{er}$ : 0 GHz

$\Omega_{er}$ : see x-axis

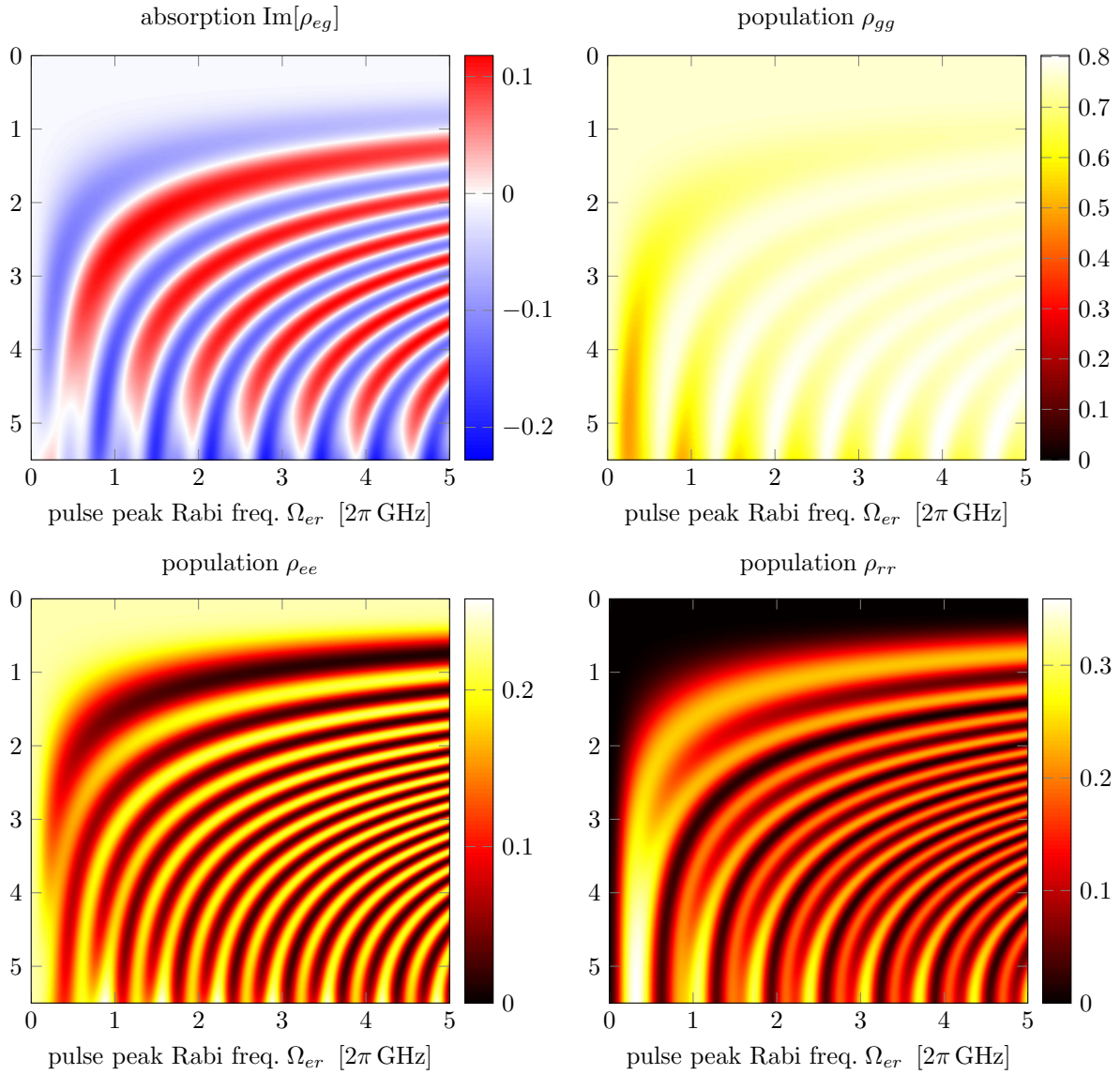


Figure B.6.: Rabi frequency scan of pulse  $\Omega_{er}$ , y-axis: time [ns]

# Bibliography

- [1] R. Feynman. *Simulating physics with computers*. International Journal of Theoretical Physics, 21:467–488, 1982.
- [2] D. Deutsch. *Quantum Theory, the Church-Turing Principle and the Universal Quantum Computer*. Proceedings of the Royal Society of London. A. Mathematical and Physical Sciences, 400(1818):97–117, 1985.
- [3] P. W. Shor. *Polynomial time algorithms for prime factorization and discrete logarithms on a quantum computer*. SIAM J. Sci. Statist. Comput., 26:1484, 1997.
- [4] J. I. Cirac and P. Zoller. *Quantum Computations with Cold Trapped Ions*. Phys. Rev. Lett., 74(20):4091–4094, May 1995.
- [5] D. P. DiVincenzo. *Two-bit gates are universal for quantum computation*. Phys. Rev. A, 51(2):1015–1022, Feb 1995.
- [6] Wolfgang Harneit. *Fullerene-based electron-spin quantum computer*. Phys. Rev. A, 65(3):032322, Feb 2002.
- [7] Daniel Loss and David P. DiVincenzo. *Quantum computation with quantum dots*. Phys. Rev. A, 57(1):120–126, Jan 1998.
- [8] R. Löw and T. Pfau. *Magneto-optics: Hot atoms rotate light rapidly*. Nature Photonics, 3:197–199, 2009.
- [9] D. Jaksch, J. I. Cirac, P. Zoller, S. L. Rolston, R. Côté, and M. D. Lukin. *Fast Quantum Gates for Neutral Atoms*. Phys. Rev. Lett., 85(10):2208–2211, Sep 2000.
- [10] M. D. Lukin, M. Fleischhauer, R. Cote, L. M. Duan, D. Jaksch, J. I. Cirac, and P. Zoller. *Dipole Blockade and Quantum Information Processing in Mesoscopic Atomic Ensembles*. Phys. Rev. Lett., 87(3):037901, Jun 2001.

- [11] M. Saffman, T. G. Walker, and K. Mølmer. *Quantum information with Rydberg atoms*. Rev. Mod. Phys., 82(3):2313–2363, Aug 2010.
- [12] J. Pritchard. *Cooperative Optical Non-linearity in a blockaded Rydberg Ensemble*. PhD thesis, Durham University, 2011.
- [13] C. Cohen-Tannoudji. *Amazing Light: A Volume Dedicated to Charles Hard Townes on His 80th Birthday*, chapter The Autler-Townes effect revisited, page 109. SPIE Society of Photo-Optical Instrumentation Engi, 1996.
- [14] E. Bäder. *Pulsed Rydberg spectroscopy in thermal vapor of rubidium*. Diploma thesis, Universität Stuttgart, 5. Physikalisches Institut, 2010.
- [15] S. Müller. *Nonlinear Optics involving Rydberg States in a Rubidium Vapour Cell*. Diploma thesis, Universität Stuttgart, 5. Physikalisches Institut, 2008.
- [16] N. Bohr. *On the Constitution of Atoms and Molecules*. Phil. Mag., 26:1–24, 1913.
- [17] E. Schrödinger. *An Undulatory Theory of the Mechanics of Atoms and Molecules*. Phys. Rev., 28(6):1049–1070, Dec 1926.
- [18] T. F. Gallagher. *Rydberg atoms*. Rep. Prog. Phys., 51:143, 1988.
- [19] L. Allen and J. H. Eberly. *Optical resonance and two-level atoms*. Dover books on physics and chemistry. Dover, 1987.
- [20] C. Cohen-Tannoudji, J. Dupont-Roc, and G. Grynberg. *Atom-photon interactions: basic processes and applications*. Wiley science paperback series. Wiley, 1998.
- [21] I. I. Rabi. *Space Quantization in a Gyating Magnetic Field*. Phys. Rev., 51(8):652–654, Apr 1937.
- [22] G. Lindblad. *On the generators of quantum dynamical semigroups*. Communications in Mathematical Physics, 48:119–130, 1976.
- [23] H. Helm. *Dissipative processes in light-atom interactions*. Lecture Notes, SS 2008.
- [24] H. Kübler, J. P. Shaffer, T. Baluktsian, R. Löw, and T. Pfau. *Coherent excitation of Rydberg atoms in micrometre-sized atomic vapour cells*. Nature Photonics, 4:112–116, 2010.

- [25] Z. Hadzibabic. *Studies of a Quantum Degenerate Fermionic Lithium Gas*. PhD thesis, Massachusetts Institute of Technology, 2003.
- [26] S. Imanishi, U. Tanaka, and S. Urabe. *Frequency Stabilization of Diode Laser Using Dichroic-Atomic-Vapor Laser Lock Signals and Thin Rb Vapor Cell*. Japanese Journal of Applied Physics, 44(9A):6767–6771, 2005.
- [27] F. E. Becerra, R. T. Willis, S. L. Rolston, and L. A. Orozco. *Two-photon dichroic atomic vapor laser lock using electromagnetically induced transparency and absorption*. J. Opt. Soc. Am. B, 26(7):1315–1320, Jul 2009.
- [28] D. A. Steck. *Rubidium 85 D Line Data*, 2010.
- [29] D. A. Steck. *Rubidium 87 D Line Data*, 2010.
- [30] E. S. Lee and J. W. Hahn. *Four-pass amplifier for the pulsed amplification of a narrow-bandwidth continuous-wave dye laser*. Opt. Lett., 21(22):1836–1838, Nov 1996.
- [31] A. Schwettmann, C. McGuffey, S. Chauhan, K. R. Overstreet, and J. P. Shaffer. *Tunable four-pass narrow spectral bandwidth amplifier for use at  $\sim 508$  nm*. Appl. Opt., 46(8):1310–1315, Mar 2007.
- [32] J. W. Hahn and Y. S. Yoo. *Suppression of Amplified Spontaneous Emission from a Four-Pass Dye Laser Amplifier*. Appl. Opt., 37(21):4867–4870, Jul 1998.
- [33] A. Kölle. *Aufbau eines gepulsten bandbreitenlimitierten Laserverstärkers zum Einsatz in der kohärenten Rydbergspektroskopie*. Diploma thesis, Universität Stuttgart, 5. Physikalisches Institut, 2010.
- [34] M. Saffman and T. G. Walker. *Creating single-atom and single-photon sources from entangled atomic ensembles*. Phys. Rev. A, 66(6):065403, Dec 2002.
- [35] E. Urban, T. A. Johnson, T. Henage, L. Isenhower, D. D. Yavuz, T. G. Walker, and M. Saffman. *Observation of Rydberg blockade between two atoms*. nature physics, 5, 2009.
- [36] J. P. Shaffer. Preliminary calculations of rubidium molecules for the 35S, 45S and 55S state. Private communication.



- [37] R. Heidemann, U. Raitzsch, V. Bendkowsky, B. Butscher, R. Löw, L. Santos, and T. Pfau. *Evidence for Coherent Collective Rydberg Excitation in the Strong Blockade Regime*. Phys. Rev. Lett., 99(16):163601, Oct 2007.
- [38] H. Kübler, J. P. Shaffer, T. Baluktsian, R. Löw, and T. Pfau. *Coherent excitation of Rydberg atoms in micrometre-sized atomic vapour cells*. Nature Photonics, 4:112–116, 2010.
- [39] J. Honer, R. Löw, H. Weimer, T. Pfau, and H. P. Büchler. *Artificial atoms can do more than atoms: Deterministic single photon subtraction from arbitrary light fields*. ArXiv e-prints, March 2011.
- [40] R. Daschner. *Frequenzmodulationsspektroskopie von Rydberg-Zuständen in Rubidium-Mikrozellen*. Diploma thesis, Universität Stuttgart, 5. Physikalisches Institut, 2011.
- [41] A. Batär. *Effiziente Erzeugung ultrakalter Rubidiumatome*. Diploma thesis, Universität Stuttgart, 5. Physikalisches Institut, 2001.